Check for updates

Received: 18 December 2021 | Revised: 15 July 2022 | Accepted: 18 July 2022

DOI: 10.1002/esp.5456

RESEARCH ARTICLE

ESPL WILEY

Age, formation and significance of loess deposits in central Sweden

Thomas Stevens[1] | Daniele Sechi[2] | Charilaos Tziavaras[1] | Ramona Schneider[1] | Adriano Banak[3] | Stefano Andreucci[4] | Martina Hättestrand[5] | Vincenzo Pascucci[2,6]

[1]Department of Earth Sciences, Uppsala University, Uppsala, Sweden

[2]Department of Architecture, Design and Planning, University of Sassari, Alghero, Italy

[3]Department for Geology, Croatian Geological Survey, Zagreb, Croatia

[4]Dipartimento di Scienze Chimiche e Geologiche, Università degli Studi di Cagliari, Cittadella Universitaria (Blocco A), Monserrato, Italy

[5]Department of Physical Geography, Stockholm University, Stockholm, Sweden

[6]Institute of Geology and Petroleum Technologies, Kazan Federal University, Kazzan, Russia

Correspondence
Thomas Stevens, Department of Earth Sciences, Uppsala University, Villavägen 16, Uppsala 75236, Sweden.
Email: thomas.stevens@geo.uu.se

Funding information
Swedish Research Council, Grant/Award Number: 2017-03888; Swedish Geological Survey, Grant/Award Number: 6-1857/2020

Abstract

Loess deposits are common in the mid-latitudes and are excellent records of past climate, landscape change and dust. However, loess deposits are seldom reported from Fennoscandia. Here we investigate two former glaciofluvial areas in central Sweden, Brattforsheden and Bonäsheden, where post-glacial loess and sand dune activity have been documented previously. Based on detailed mapping, grain size, scanning electron microscopy and optically stimulated luminescence dating analyses, we confirm the presence of loess deposits at the sites and extend the known area of loess coverage. Our results suggest that loess deposits are more common than previously thought in Sweden. The results also demonstrate that basal parts of the loess are often mixed with underlying sediment, which may be a common feature of thin loess deposits close to former ice margins. Quartz luminescence is well suited for dating these deposits, but ages from the mixed basal loess layers are older than expected, while ages from undisturbed loess extend to c. 5 ka. The loess ages contrast with the timing of main dune activity in these areas, which is dominantly in the 1–3 kyr post-deglaciation (c. 10.9–10.5 cal kyr BP). We suggest that either sediment mixing during soil formation is responsible for the mid-Holocene loess ages, or that the loess deposits record periodic landscape destabilization into the mid-Holocene. Furthermore, there is a clear topographic control on aeolian sedimentary facies, with loess mantling high ground and dunes restricted to valleys. Loess deposits are also primarily found to the south and southwest of source areas, implying transport from the north and east. This pattern contrasts with evidence for NW winds inferred from associated sand dunes. At present, the reasons for this mismatch are unclear, although one possible explanation is that silts deposited at higher elevations were affected by Ekman flow deflection of NW surface winds.

KEYWORDS
aeolian, Holocene, luminescence, OSL, Quaternary, SEM

1 | INTRODUCTION

Loess deposits comprise homogeneous, dominantly silt size, siliciclastic, windblown sediments that blanket the underlying terrain (Pye, 1995; Schaetzl et al., 2018). Sequences of loess are widespread, covering around 10% of the world's land area (Pécsi, 1991), and form globally important Quaternary–Neogene climate archives. Loess deposits are widespread and well studied in vast areas of Asia and Central Europe (Lehmkuhl et al., 2021; Lu et al., 2022; Schaetzl et al., 2018). In Central Europe, away from the margins of former ice limits, loess deposits are common and reach tens of metres thick (Lehmkuhl et al., 2021), stretching back over a million years (Marković et al., 2011). Thick loess deposits are rarer in the higher latitudes, closer to or under former ice limits in the Late Quaternary, and are

This is an open access article under the terms of the Creative Commons Attribution License, which permits use, distribution and reproduction in any medium, provided the original work is properly cited.
© 2022 The Authors. *Earth Surface Processes and Landforms* published by John Wiley & Sons Ltd.

often reworked or decalcified (Lehmkuhl et al., 2021; Schaetzl & Loope, 2008). However, loess deposits in the broad sense of terrestrial windblown dust (Muhs, 2013) also exist in many of these areas (Bryant, 1982; Jackson et al., 2005; Stevens et al., 2020; Willemse et al., 2003), even if they are generally thinner and with patchier distributions. These deposits are potentially extremely useful as climate and landscape evolution archives in the higher latitudes, one of the most sensitive areas to climate change (Overland et al., 2019).

Loess is mainly comprised of coarse (>5 μm), windblown, mineral dust particles, and atmospheric mineral dust is a fundamental component of the climate system (Knippertz & Stuut, 2014). However, this link to climate change is poorly known, especially in the past, and coarse dust has specific climate-forcing properties that are widely missed in climate modelling and monitoring (Adebiyi & Kok, 2020). Furthermore, Northern Hemisphere high-latitude dust (here defined as >50°N after Bullard et al., 2016) and its impact are particularly poorly understood (Bullard et al., 2016; Groot-Zwaaftink et al., 2016). As such, Swedish loess deposits may be important for determining the activity and impact of past coarse dust in the high latitudes. However, to fully utilize this record requires excellent constraint on distribution and depositional ages, as well as loess properties.

1.1 | Loess in Sweden

Loess deposits (*sensu* wind-blown terrestrial dust) have been suggested to occur at some locations in central Sweden (Agrell & Hultman, 1971; Ekström & Hedeving, 2021; Hjulström et al., 1955; Hörner, 1927). Hörner (1927) first mapped what he suggested to be windblown loess deposits (termed *flygmo*) around the perimeter of a former glaciofluvial meltwater channel and delta at Brattforsheden (Figures 1 and 2). He argued that the position of loess on high ground, the lack of sedimentary structure, dominant silt size, association with aeolian dunes and tendency to bury all other features suggested an aeolian origin. These deposits, up to a metre thick, sparked later discussion (see Hjulström et al., 1955) about the type of winds that transported this material, and the timing of deposition. Hjulström et al. (1955) also mapped suspected loess deposits further north, just west of the Bonäsheden glaciofluvial delta system and aeolian dune field (Figures 1 and 3). These deposits share many sedimentary and geomorphic properties and associations to those at Brattforsheden, suggesting a causal link between glaciofluvial, aeolian dune, cover sand and loess systems during the demise of the last Fennoscandian Ice Sheet (Hjulström et al., 1955). Possible sporadic loess deposits have also been discovered in southern Sweden, both at Svartedalen (Ekström & Hedeving, 2021) and in the southern Swedish uplands (Agrell & Hultman, 1971) (Figure 1). Again, both these deposits are located close to former glaciofluvial meltwater channels or deltas, active during the last deglaciation.

Since the early work on Swedish loess, most aeolian geomorphology and sedimentology work in Sweden has focused on sand dunes and fine dust (mostly <5 μm) in peat bogs (Alexanderson et al., 2016; Kylander et al., 2018). However, there is great potential in investigating the possible Swedish loess archives, which provide a record of

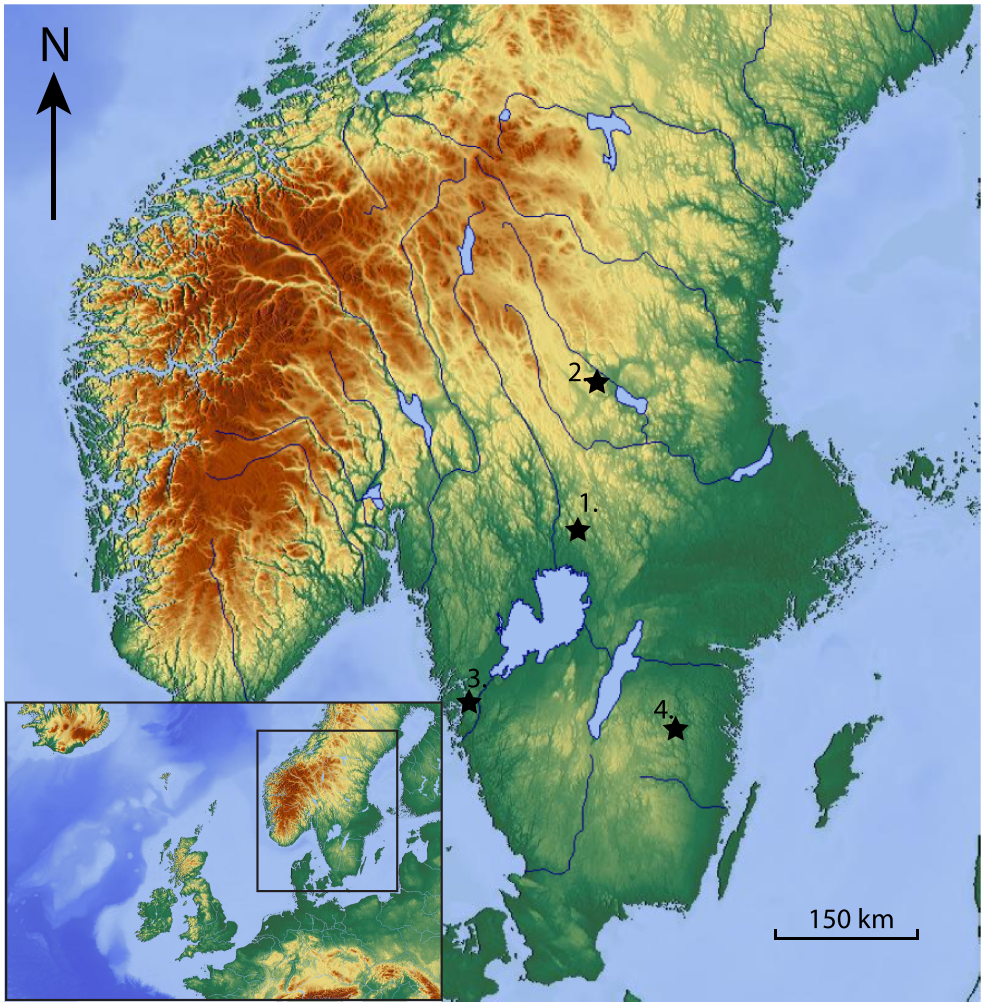

FIGURE 1 Overview of southern Sweden showing four documented areas with likely loess deposits marked with stars. 1 = Brattforsheden; 2 = west of Bonäsheden; 3 = Svartedalen; 4 = southern Swedish uplands [Color figure can be viewed at wileyonlinelibrary.com]

10969837, 2022, 14, Downloaded from https://onlinelibrary.wiley.com/doi/10.1002/esp.5456 by CochraneItalia, Wiley Online Library on [19/12/2024]. See the Terms and Conditions (https://onlinelibrary.wiley.com/terms-and-conditions) on Wiley Online Library for rules of use; OA articles are governed by the applicable Creative Commons License

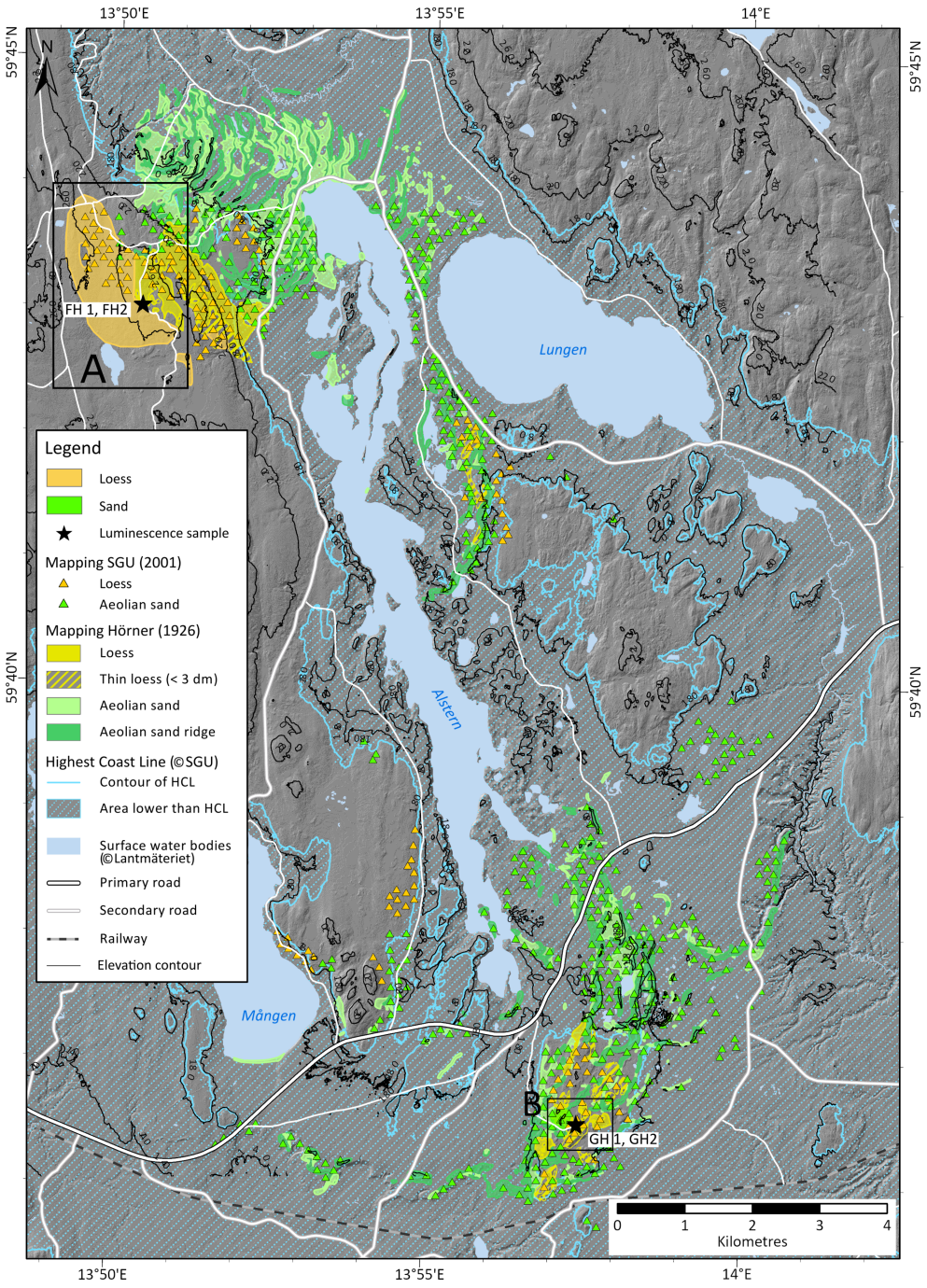

FIGURE 2 Overview of aeolian sediments and landforms at Brattforsheden, Värmland. Existing loess and aeolian sand as mapped by Hörner (1927) and Fredén (2001) at the Geological Survey of Sweden (SGU) and digitized for this study are marked alongside the highest coastline (HCL) during deglaciation (SGU, 2015), current surface water bodies and a topographic digital elevation model (DEM) (elevation data, grid 2+, © Lantmäteriet, 2019). Also shown are simplified results of further loess mapping conducted here (see Section 2). Framed areas in A and B are shown in more detail in Figure 4 [Color figure can be viewed at wileyonlinelibrary.com]

coarse dust (mostly >5 μm), allowing a more complete reconstruction of the aeolian environment. The association of loess deposits with glaciofluvial source areas and aeolian dunes can be used to reconstruct past wind directions (Hörner, 1927). However, as noted in the early studies on Swedish loess highlighted above, the position of the loess deposits poses somewhat of a conundrum (Hjulström et al., 1955). While most central Sweden parabolic dune ridge orientations suggest NW wind directions driving sand movement (Bernhardson & Alexanderson, 2018; Bernhardson et al., 2019), according to previous mapping the loess deposits tend to lie to the south or west of the main dune and glaciofluvial delta and channel areas (Figures 2 and 3), potentially suggesting dust transport by NE winds. This pattern is contrary to what would be expected if the winds that drove dune morphology were the same ones that transported the fine sands, silts and clays that form loess. This mismatch has led to a range of hypotheses being proposed to explain this pattern, including the effects of Ekman flow on higher-altitude dust-transporting winds, differential timing of dust activity versus dune movement, different seasonality in loess and sand transport, different wind systems transporting the loess and the sand (cold dry anticyclonic and intense westerly cyclonic, respectively) and even misidentification of longitudinal dunes as transverse/parabolic dunes (summarized in Hjulström et al., 1955).

Indeed, a great many fundamental questions remain. Detailed mapping, sedimentological, geochemical and mineral magnetic analyses of these sediments are mostly lacking, and although it is assumed that the deposits are loess (*sensu* wind-blown terrestrial coarse dust), this hypothesis requires further testing. Furthermore, all of the potential insight gained from these deposits noted above requires accurate, precise and independent age control, yet few

10969837, 2022, 14, Downloaded from https://onlinelibrary.wiley.com/doi/10.1002/esp.5456 by CochraneItalia, Wiley Online Library on [19/12/2024]. See the Terms and Conditions (https://onlinelibrary.wiley.com/terms-and-conditions) on Wiley Online Library for rules of use; OA articles are governed by the applicable Creative Commons License

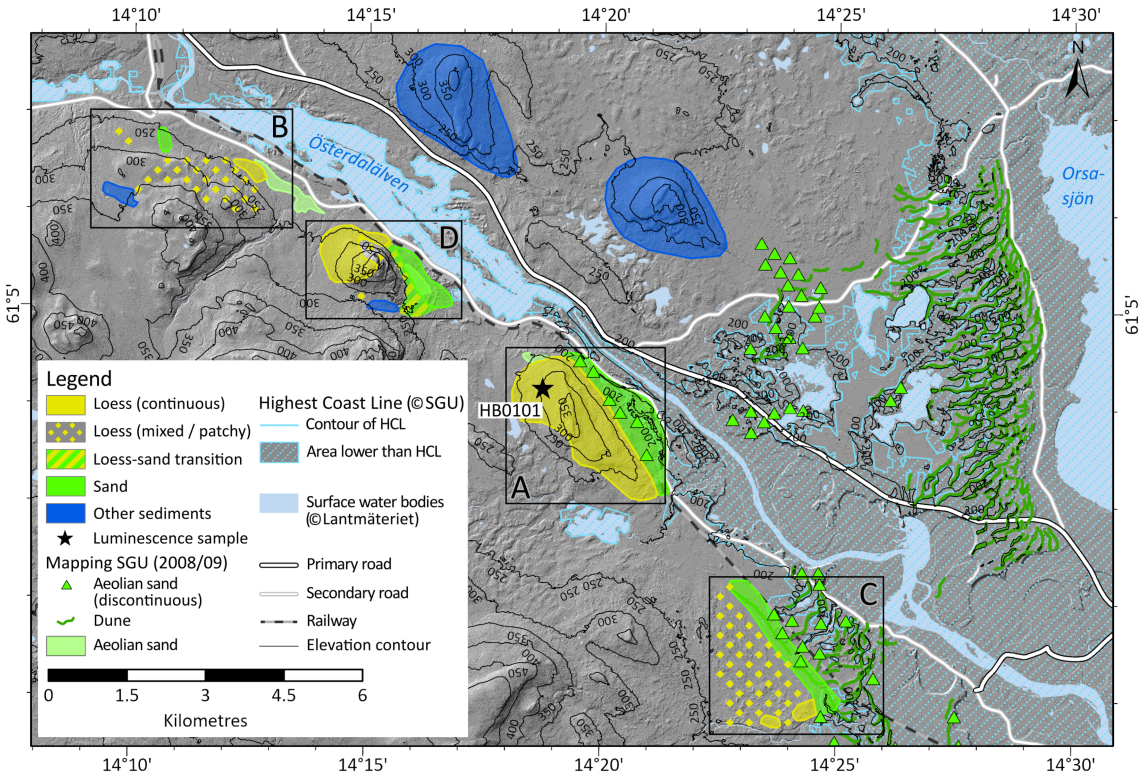

FIGURE 3 Overview of aeolian sediments and landforms at and west of the Bonäsheden dune field, Dalarna. Existing aeolian sand as mapped by Svedlund (2008a,b), Svedlund and Dahlberg (2009) and Dahlberg and Mikko (2009) at the Geological Survey of Sweden (SGU) is marked alongside the highest coastline (HCL) during deglaciation (SGU, 2015), current surface water bodies, and a topographic digital elevation model (DEM) (elevation data, grid 2+, © Lantmäteriet, 2019). Note that no loess was mapped by SGU at the site. Also shown are simplified results of further loess mapping conducted here (see Section 2) and based on the results of Hjulström et al. (1955). Framed areas A to D are shown in more detail in Figure 5 [Color figure can be viewed at wileyonlinelibrary.com]

numerical ages have been obtained from these deposits. Understanding the timing of loess deposition allows testing between some of the hypotheses over contrasting wind directions inferred from dune morphology and the position of loess deposits, and can constrain the relationship between loess activity and deglaciation, dune activity and possible landscape destabilization events.

Detailed luminescence dating has been conducted extensively on dune deposits in central Sweden. Initial thermoluminescence (TL) dating of dune sediments at both Brattforsheden and Bonäsheden by Lundqvist and Mejdahl (1987) suggested that most aeolian activity was limited to c. 1 ka immediately following deglaciation. Interestingly, the authors also provided ages for one silt sample in both areas, which yielded results essentially identical to the dune ages. However, the authors state that uncorrected feldspar fading may have affected these ages, and TL dating of aeolian sediments has a number of inherent problems that limit accurate (and certainly precise) age determination (Roberts, 2008). More recently, extensive quartz optically stimulated luminescence (OSL) dating of dunes in the Brattforsheden and Bonäsheden dune fields has been conducted (Alexanderson & Bernhardson, 2016, 2019; Alexanderson & Fabel, 2015; Bernhardson & Alexanderson, 2017). Overall, these studies point to the main phase of dune activity in central Sweden north of the Younger Dryas Middle Swedish End Moraine Zone occurring in the 1–3 ka following deglaciation or local sea-level drop. There is also evidence of an extensive reactivation phase during the late Holocene, which resulted in sand sheet deposition over the last 3 ka in many areas, possibly related to increased storminess and human activity. However, while chronological evidence from Arctic Fennoscandia points to extensive mid-Holocene dune reworking (Matthews & Seppälä, 2014), middle and early to mid-Holocene ages are relatively rare in central Sweden, implying dune stability over much of the period between 8 and 3 ka (i.e. the Northgrippian Stage, corresponding roughly to the Atlantic and Subboreal chronozones). Limited dating of the loess sediments at Brattforsheden (two ages from two sections) also suggests a similar age for these sediments (Alexanderson & Fabel, 2015).

As such, these studies broadly agree with the prevailing paradigm of relatively rapid cessation of most medium to coarse silt and sand aeolian activity following deglaciation in the early Holocene. By contrast, studies of fine windblown dust in peat bogs in southern Sweden suggest multiple dust events in the Northgrippian/mid-Holocene (Kylander et al., 2016, 2018). The earliest of these events occurred around 6.4–5.3 cal kyr BP, but multiple shorter-duration episodes occurred up until c. 3 ka, possibly involving shifts in dust source regions (Kylander et al., 2016, 2018). The apparent decoupling of fine dust accumulation and source changes with dune activity is somewhat puzzling, as it may be expected that an increase in aeolian activity generally would affect both dustiness and sand drift. The missing link in this conundrum is the loess deposits and the timing and nature of their accumulation. As such, there is a clear need for an investigation of the sedimentological properties and age of loess deposits in Sweden.

Here we test the causes and nature of post-glacial loess deposition in central Sweden with a focus on the two best known examples of loess deposits located at Brattforsheden (Värmland) and west of

10969837, 2022, 14, Downloaded from https://onlinelibrary.wiley.com/doi/10.1002/esp.5456 by CochraneItalia, Wiley Online Library on [19/12/2024]. See the Terms and Conditions (https://onlinelibrary.wiley.com/terms-and-conditions) on Wiley Online Library for rules of use; OA articles are governed by the applicable Creative Commons License

Bonäsheden (Siljan area, Dalarna; Figures 1–3). First, we ground-truth and extend previous mapping work on these deposits, and then present the results of basic sediment characterization [using scanning electron microscopy (SEM), particle size, mineral magnetism and geochemistry], together with detailed OSL dating of selected typical profiles.

2 | SITES AND METHODS

2.1 | Field area

Brattforsheden is an extensive glaciofluvial delta complex formed during the deglaciation of central Sweden at the Baltic Sea coast during the Yoldia Sea phase (Fredén, 2001) around 10.9 cal kyr BP (Stroeven et al., 2016). Mapped in detail by Hörner (1927), the delta formed at the regional highest shoreline (175–190 m a.s.l.) during deglaciation and is part of a larger area of glaciofluvial, lacustrine and aeolian deposits (Figure 2). The delta covers an area of c. 15 km^2 to the south of a structurally controlled NNW–SSE trending valley currently dominated by Lake Alstern (Alexanderson & Fabel, 2015). Aeolian sediments cover many locations in the delta and valley complex, dominantly sand dunes of crescentic–parabolic form, but also including cover sands and loess-like material (Alexanderson & Fabel, 2015; Hjulström et al., 1955; Hörner, 1927). Deglaciation has been dated via correlation to varve chronologies or ^{14}C-dated recession lines and lake sediments in the region (Fredén, 2001). Detailed OSL, ^{14}C and surface exposure (^{10}Be) dating conducted by Alexanderson and Fabel (2015) suggests deglaciation at or just before 11 ka. In addition to dune fields, the area also contains several deposits identified as loess, particularly on hills such as Finnhöjden and Gräshöjden (Figure 2).

Around 160 km further north lies another glaciofluvial complex that follows the course of the modern Österdalälven River and terminates in the Mora glaciofluvial delta (Figure 3). This delta system formed around 210–215 m a.s.l. (Nordell, 1984), close to the highest shoreline of the Ancylus Lake phase of the Baltic, at around 10.5 cal kyr BP (Stroeven et al., 2016). On top of part of the delta lies the Bonäsheden dune field, Sweden's largest continuous dune field. A striking line marking the eastern end of this field marks the former elevated lake level of Ancient Lake Siljan (Orsasjön; Figure 3). Dunes and cover sand deposits also exist along the valley sides further to the west (Figure 3). Thin loess deposits have been reported by Hjulström et al. (1955) to lie on Hökberg, 5–10 km west of Bonäsheden dune field, as well as on some adjacent hills to the southwest of the Österdalälven River (Figure 3).

2.2 | Fieldwork and mapping

Multiple trips were conducted between autumn 2018 and summer 2021 to map and characterize the loess and associated sediment at Brattforsheden (Värmland) and west of Bonäsheden (Dalarna) (Figures 1–3). As well as mapping, representative loess sequences on hill tops were sampled for luminescence dating and basic sediment characterization using SEM, particle size, mineral magnetism and geochemistry. Mapping was conducted to characterize the distribution, thickness and grain size composition of loess sediment in both field areas, and to test previous observations on loess coverage (Fredén, 2001; Hjulström et al., 1955; Hörner, 1927). Areas previously mapped both with and without loess coverage were examined. Mapping was conducted by soil auguring over multiple transects, considering terrain, previous mapping and topography. A two-frequency carrier-phase GNSS receiver (Trimble R7) was used to position sampling points, and broad sediment type was qualitatively assessed [sand, silt (possible loess), peat, etc.] at each point. Sediments a few centimetres thick were considered in the mapping, which differs from the Geological Survey of Sweden (SGU), which generally only maps sediment deposits >50 cm. The collected data were post-processed against the SWEPOS network stations in Mora, Molkom and Filipstad as base stations. Processing was undertaken using Trimble Business Center software (v3.7) with subdecimetre-scale accuracy. Where loess or loess-like material was observed, a sample for particle size analysis was collected immediately below the A-horizon, and the loess thickness was assessed where possible. Mapping of loess thickness and grain size data was conducted using Esri ArcGIS Pro and Inkscape. Representative sections or soil pits were also dug into loess deposits from each area to examine loess stratigraphy and to sample for luminescence dating and sediment characteristics. Each section was cleaned, logged and described in detail, and samples for sediment analysis and luminescence dating were taken at regular intervals (varying between site and section depending on access, stones in the profile and profile thickness, see below).

2.3 | Magnetic susceptibility

Magnetic susceptibility at low field frequencies (χlf) measures the total ferri- and ferromagnetic assemblage in a sediment, while higher measurement frequencies (χhf) exclude portions of the finer-grained (0 to c. 0.03 μm-diameter) superparamagnetic (SP) grains (Dearing et al., 1996). The frequency dependence of magnetic susceptibility can therefore yield information about the influence of fine-grained SP grains on the magnetic susceptibility signal, and in many instances is used as an indicator of various environmental effects (Bradák et al., 2021; Maher & Taylor, 1988). After drying and weighing, mass-corrected magnetic susceptibility was measured on all loess samples using an Agico Kappabridge MFK1-FA at Uppsala University. Each sample was measured three times at 976 Hz (χlf) and 15 616 Hz (χhf) (Hrouda, 2011) in a peak field of 200 A m^{-1}, and the mean was used to calculate mass-dependent susceptibility (in m^3 kg^{-1}). A reference sample with known magnetic susceptibility was also measured at both frequencies to check instrument drift during measurement. Frequency dependence as a percentage χfd (%) was calculated by the following relationship:

$$\chi\text{fd}\,(\%) = [(\chi\text{lf} - \chi\text{hf})/\chi\text{lf}] \times 100$$

while frequency dependence, as the difference between χlf and χhf ($\Delta\chi$), is simply

$$\Delta\chi\left(\text{m}^3\,\text{kg}^{-1}\right) = \chi\text{lf} - \chi\text{hf}$$

In order to easily compare frequency dependence between samples measured on magnetic susceptibility equipment with different

10969837, 2022, 14, Downloaded from https://onlinelibrary.wiley.com/doi/10.1002/esp.5456 by CochraneItalia, Wiley Online Library on [19/12/2024]. See the Terms and Conditions (https://onlinelibrary.wiley.com/terms-and-conditions) on Wiley Online Library for rules of use; OA articles are governed by the applicable Creative Commons License

measurement frequency, the normalized version of frequency dependence, χfn, is preferable to χfd, as defined by Hrouda (2011):

$$\chi fn\,(\%) = \chi fd/(\ln Fhf - \ln Flf)$$

where Fhf and Flf are the high and low operating frequencies used by the magnetic susceptibility meter, respectively.

2.4 | Grain size

Grain size analysis is a powerful tool in assessing the nature of aeolian transport and potential reworking in loess sediments (Schaetzl & Attig, 2013; Újvári et al., 2016; Vandenberghe, 2013). Samples for grain size analysis were oven dried at 50°C for 24 h and delicately homogenized to break down larger aggregates. Subsamples of c. 3 g were then treated with 12% HCl to remove carbonates and 33% H_2O_2 to remove organic matter. Samples were immersed in 0.5% $(NaPO_3)_6$ and ultrasonicated briefly prior to analysis. Grain size distributions were measured by three repeat measurements on a Malvern Mastersizer X at Uppsala University with a He–Ne laser ($\lambda = 632.8$ nm) under the polydispersive model and using a 300 mm lens capable of detection of 1.2–600 μm particles. The average distributions were then used in further analyses after the exclusion of obvious outliers. Although complicated by factors such as source distance and sediment availability (Újvári et al., 2016), grain size distribution shape can help determine loess transport and depositional processes (Vandenberghe, 2013). In addition to distribution statistics and percentage of different grain size classes, the U ratio was also calculated (Vandenberghe & Nugteren, 2001). The U ratio is the ratio of the percentage of 16–44 μm fraction to the percentage of 5.5–16 μm fraction and is designed to exclude grains formed during *in-situ* weathering and grains transported by local saltation. Arguably, then, the U ratio is a better indicator of the intensity of wider-scale aeolian suspension activity, with higher values denoting stronger winds or a more dynamic aeolian environment.

2.5 | Elemental geochemistry

Sample geochemistry provides insights into weathering, source change and grain size change. Elemental/oxide chemistry was determined by X-ray fluorescence spectroscopy (XRF). Samples were first oven dried at 50°C for 12 h minimum and then pulverized to a powder using a quartz mill and packed into Bruker measuring containers covered with Prolene film prior to measurement on a Bruker TRACER 5i used in fixed laboratory position at Uppsala University. In-built GeoMining and GeoExploration calibrations were used to obtain the majority of element/oxide concentrations, empirically corrected for known offsets obtained from known concentration samples. NaO, MgO and Al_2O_3 are unmeasurable or do not perform well with the in-built tracer calibrations. As such, a specific calibration was created for these oxides using Bruker EasyCal software and a group of known concentration samples after measurement via sodium peroxide ICP-MS and wavelength dispersive XRF at SGS Minerals Canada. Under this calibration, samples were measured in He atmosphere with no filter window. Each sample was measured three times, and the average was used for further analysis. All abundant elements are presented as oxides irrespective of machine output, and major oxides were summed and normalized to 100%. The oxide concentrations used to determine weathering indices (see below) were calculated according to their molar masses.

The Chemical Index of Alteration (CIA) (Nesbitt & Young, 1982) was used to yield a quantitative measure of feldspar weathering. In the case of weathering intense enough to alter K-feldspar and plagioclase, the mobile elements Na, Ca and K should all be removed, leading to enrichment of the immobile element Al (Buggle et al., 2011). A higher value of the index therefore indicates increased weathering, as defined:

$$CIA = [mAl_2O_3/(mAl_2O_3 + mCaO^* + mNa_2O + mK_2O)] \times 100$$

where m denotes molar mass and CaO* is the assumed CaO content from silicate minerals, in order to remove the influence of CaO from carbonates and phosphates. If the CaO value is lower or equal to Na_2O then the former value is used, while if CaO is higher than Na_2O then the Na_2O value is used instead.

2.6 | Scanning electron microscopy

Quartz grains were imaged in order to see the shape of the grains and their detailed grain surface morphology. The photographs were made using a JEOL JSM-35 scanning electron microscope in the laboratory of the Croatian Geological Survey in Zagreb. Twelve samples from the loess sections and pits were prepared for SEM and nine were analysed from the different sections. The heavy mineral fraction was first extracted from the samples, and the light fraction was analysed. More than 600 different grains were photographed under SEM, and the best photographs showing complete quartz grains were selected. Microscopy was made within a magnification range of 200× to 1800×. Selected grains were mounted onto double-sided adhesives and then coated with a 15 nm gold layer. The classification of quartz grain surface microtexture and terminology used here is based on Mahaney (1995, 2002) and Strand et al. (2003).

2.7 | Luminescence dating: sample treatment and facilities

Samples for luminescence dating were obtained by hammering c. 10–20 cm-long, 4 cm-diameter steel tubes into the cleaned exposures. Water contents and dose rates were measured on sediment extracted from holes after tube removal. Samples were processed for luminescence dating in the Laboratory for Luminescence Dating at the University of Sassari, Sardinia, Italy and the Luminescence Dating Laboratory at Stockholm University. Sample tubes were opened under subdued red light. The outer 5 cm of sediment was scraped off, and the inner material not exposed to light was used for luminescence dating. This material was then treated with 15–40% HCl and 15–30% H_2O_2 to remove carbonate and organic matter, respectively, and wet sieved at different grain size ranges. The grain size fraction 60–90 mm was chosen for D_e measurement, and pure quartz grains were extracted from the total fraction by two-step heavy liquid separation

10969837, 2022, 14, Downloaded from https://onlinelibrary.wiley.com/doi/10.1002/esp.5456 by CochraneItalia, Wiley Online Library on [19/12/2024]. See the Terms and Conditions (https://onlinelibrary.wiley.com/terms-and-conditions) on Wiley Online Library for rules of use; OA articles are governed by the applicable Creative Commons License

with sodium polytungstate (2.70 g cm^3; 2.62 g cm^3). Quartz grains were then soaked in 40% HF for at least 1 h to remove remaining K-feldspar grains and etch the quartz α-irradiated rims (Porat et al., 2015). Finally, samples were rinsed and kept in a 40% HCl bath overnight to remove all fluoride precipitates.

All luminescence analyses were carried out using a Risø TL/OSL-DA-20 reader equipped with calibrated $^{90}Sr/^{90}Y$ beta sources (of ~0.114 Gy s^{-1}) at the Laboratory for Luminescence Dating at the University of Sassari. Multi-grain small aliquots (~200 grains) were mounted on stainless steel discs 0.9 mm in diameter and 0.2 mm in thickness using silicone spray (Duller, 2008). These quartz aliquots were stimulated using blue light-emitting diodes (LEDs) (470 nm; c. 80 mW cm^2), and the resulting OSL signal was detected through a 7.5 mm UV glass filter (Hoya U-340). A modified single-aliquot regenerative dose (SAR) protocol was used to determine the quartz OSL equivalent doses (D_e) (Murray & Wintle, 2000, 2003). The fast component of net quartz OSL was isolated using the first 0.8 s of signal with the following 0.8–2 s subtracted as background (Cunningham & Wallinga, 2010). At least 24 aliquots for each sample were analysed for D_e measurement. The performance of the SAR protocol and the quality of measurements were monitored through dose recovery tests and standard aliquot rejection criteria: (i) recycling ratio (ratio between two identical regeneration points); (ii) recuperation (signal from a zero-dose regeneration point); and (iii) natural signal <3σ above background (Wintle & Murray, 2006). The sensitivity-corrected dose–response curve for each signal was fitted using a single exponential function (to obtain the saturation value $2D_0$ of the natural D_e). Only those aliquots capable of measuring the dose of interest (i.e. with sufficiently large D_0) were considered for D_e calculation. Aliquots with 2 D_0 < D_e (D_e average of all aliquots) were considered saturated and thus rejected and not included in the palaeodose estimation (Cocco et al., 2019; Ferranti et al., 2021; Sechi et al., 2020; Stevens et al., 2020; Thomsen et al., 2016).

For water content measurement (expressed as a fraction of sample weight in %), 50–150 g of each sample was weighed and then dried in an oven at 105°C for 48 h. Following this drying, the samples were weighed again to measure the loss of water (dry weight/initial weight), yielding the natural water content (*in situ*). Water was then added until plastic limit behaviour was achieved (saturation limit). After 24 h, the saturated weight was measured (sat weight/dry weight) to obtain saturation water content.

Dose rates per sample were obtained by measuring U, Th and K concentrations after milling and via sodium peroxide fusion ICP-MS at SGS Minerals, Canada. The radionuclide concentrations were converted to dry dose rates using the conversion factors provided by Guérin et al. (2011). An internal dose rate from U and Th of 0.02 ± 0.01 Gy ka^{-1} was assumed based on Vandenberghe et al. (2008). The contribution of cosmic rays to the total dose rate was calculated according to Prescott and Hutton (1994).

3 | RESULTS

3.1 | Mapping; distribution, thickness and grain size

Figures 4 and 5 show the detailed results of our mapping conducted at specific areas in Brattforsheden and west of Bonäsheden, respectively, alongside previously published mapping results. Overview maps of the wider areas, including positions of close-up maps in Figures 4 and 5, are shown in Figures 2 and 3, respectively. Volume-weighted means (31 classes) are shown in Figures 4 and 5 as modal values of

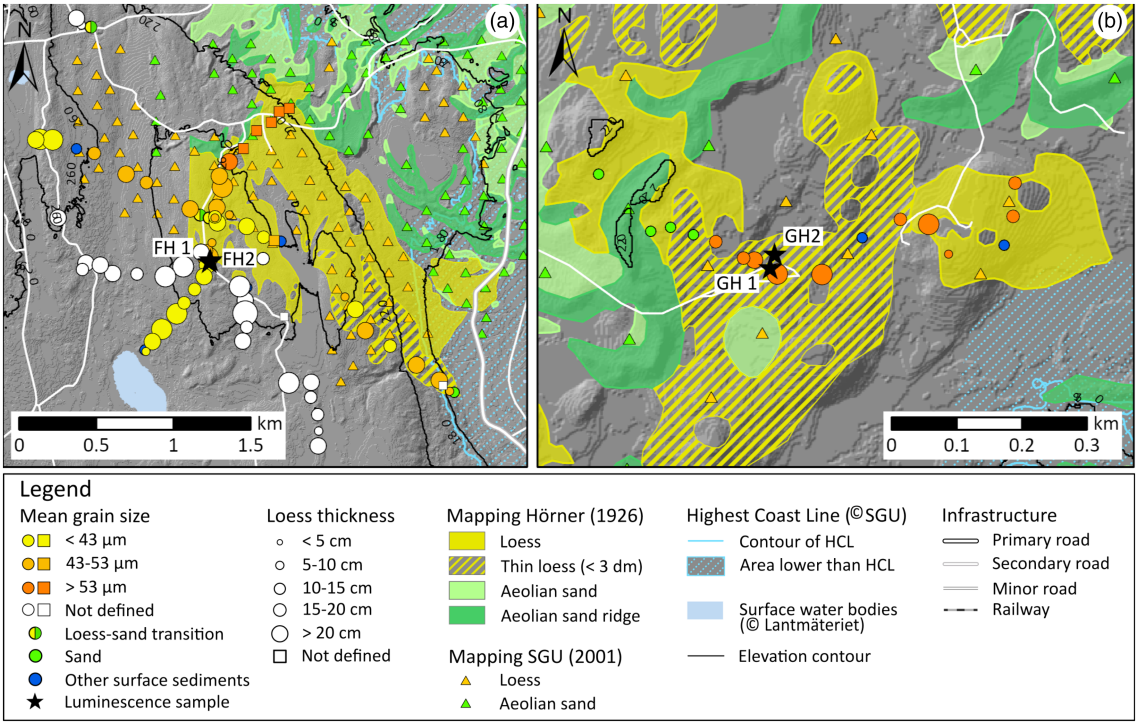

FIGURE 4 Results of mapping of loess deposits in Brattforsheden, Värmland alongside previous mapping results, highest coastline, topography and modern water bodies (see Figure 2). (A) Results from Finnhöjden. (B) Results from Gräshöjden. For location, see overview maps in Figures 1 and 2. Background image: elevation data, grid 2+, © Lantmäteriet (2019) [Color figure can be viewed at wileyonlinelibrary.com]

10969837, 2022, 14, Downloaded from https://onlinelibrary.wiley.com/doi/10.1002/esp.5456 by CochraneItalia, Wiley Online Library on [19/12/2024]. See the Terms and Conditions (https://onlinelibrary.wiley.com/terms-and-conditions) on Wiley Online Library for rules of use; OA articles are governed by the applicable Creative Commons License

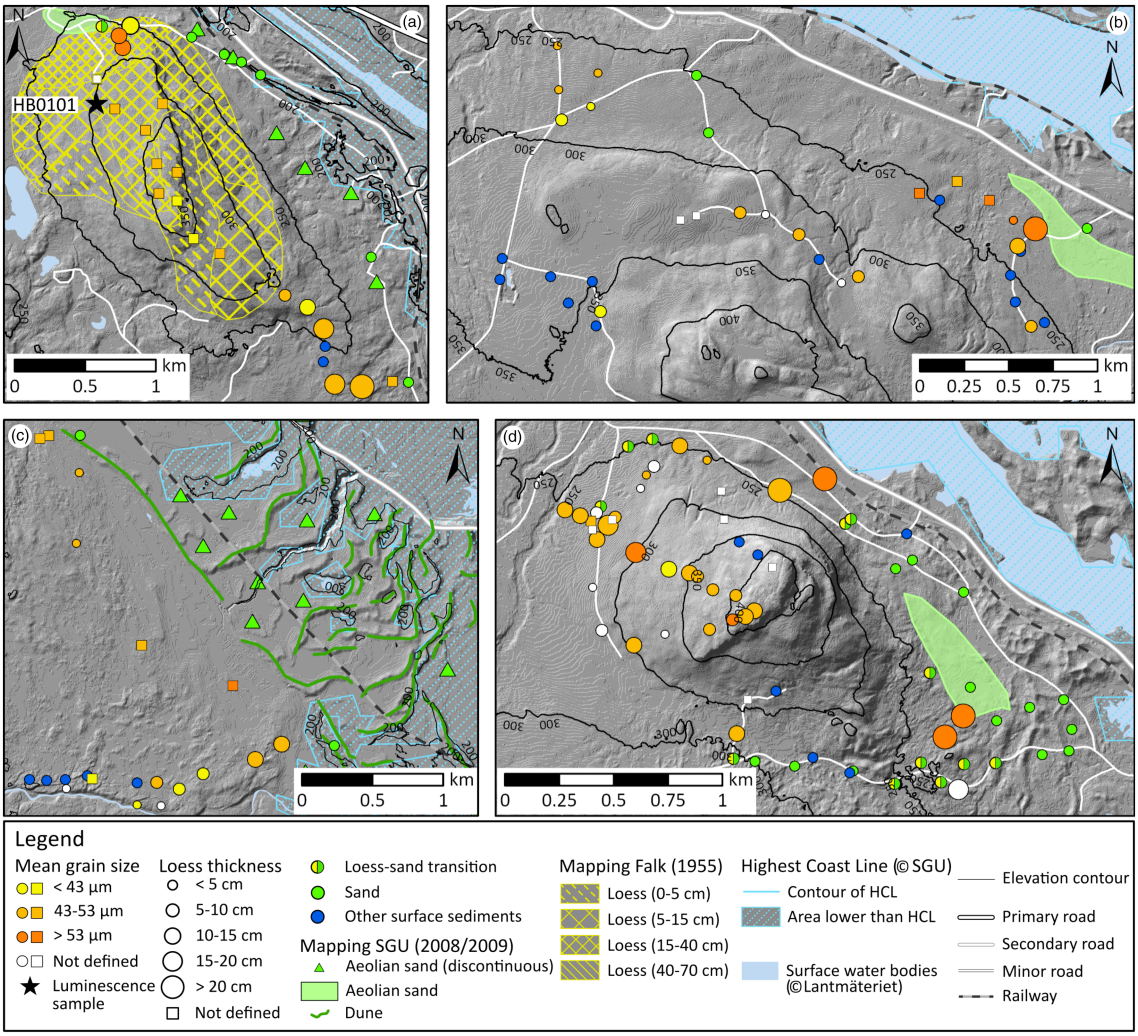

FIGURE 5 Results of mapping of loess deposits west of Bonäsheden alongside previous mapping results, highest coastline, topography and modern water bodies (see Figure 3). Results from: (A) Hökberg; (B) Oxberg; (C) Eldris; (D) Gopsberg. For location, see overview maps in Figures 1 and 3. Background image: elevation data, grid 2+, © Lantmäteriet (2019) [Color figure can be viewed at wileyonlinelibrary.com]

thin loess sediments are sometimes affected by the presence of non-loessic material mixed in from underlying sediments (see Section 4).

The loess mapped previously at Brattforsheden is variably spread over a wide area almost entirely above the highest last deglacial shoreline (Figure 2). The two main areas of loess coverage lie to the north (Finnhöjden; Figure 4A) and south (Gräshöjden; Figure 4B) of the delta complex, while the main loess area at Finnhöjden lies west of the delta complex and overlying dunes (Figure 2). The loess deposits tend to be located on hill tops and are closely associated with cover sands and sand dune complexes in the valley. Our detailed mapping of the area around the Finnhöjden hill shows that loess deposits extend well beyond previous mapping limits, and even beyond our mapping (Figure 4A). The thickness varies, with a maximum of 50–60 cm and the majority between 10 and 20 cm thick. The thinner deposits (<50 cm) would not have been mapped by SGU, which may explain some of the differences in mapping results. The thickest deposits at Finnhöjden tend to lie close to the top of the hill and eastwards, and these are also the coarsest deposits, with modes exceeding 50 µm. These deposits increase in grain size northeastwards and downslope, grading into cover sands. Further to the west and south, away from the cover sands and dunes, the mean grain size decreases to <40 µm (Figure 4A). At Gräshöjden, spatial trends are less clear and the loess is generally much coarser (Figure 4B).

Grain size distributions from samples taken in the mapping area are plotted by altitude and latitude, respectively (presented in Figures 6 and 7). These distributions generally confirm that (a) loess at the sites in Brattforsheden becomes coarser grained further north at both sites (Figure 7) and (b) at Finnhöjden there is a clear trend to finer-grained loess at higher elevations (Figure 6). The latter trend is not clear at Gräshöjden, however (Figure 6). Trends in grain size with longitude can also be seen (Figure S1), with generally finer loess further west.

As with Brattforsheden, loess west of Bonäsheden is sporadically spread over a wide area, but entirely above the highest shoreline (Figure 3). Loess distribution shows a clear spatial trend, with deposits found entirely to the southwest of the glaciofluvial system and delta, and the modern Österdalälven River. The main loess deposits are concentrated on and around hills southwest of the modern rivers, with the most extensive deposits apparently occurring around Hökberg. The areas around Hökberg, Oxberg, Eldris and Gopsberg are shown in detail in Figures 5A–D, respectively, and clearly show coverage of loess on higher ground, grading to cover sands to the east and on

10969837, 2022, 14, Downloaded from https://onlinelibrary.wiley.com/doi/10.1002/esp.5456 by CochraneItalia, Wiley Online Library on [19/12/2024]. See the Terms and Conditions (https://onlinelibrary.wiley.com/terms-and-conditions) on Wiley Online Library for rules of use; OA articles are governed by the applicable Creative Commons License

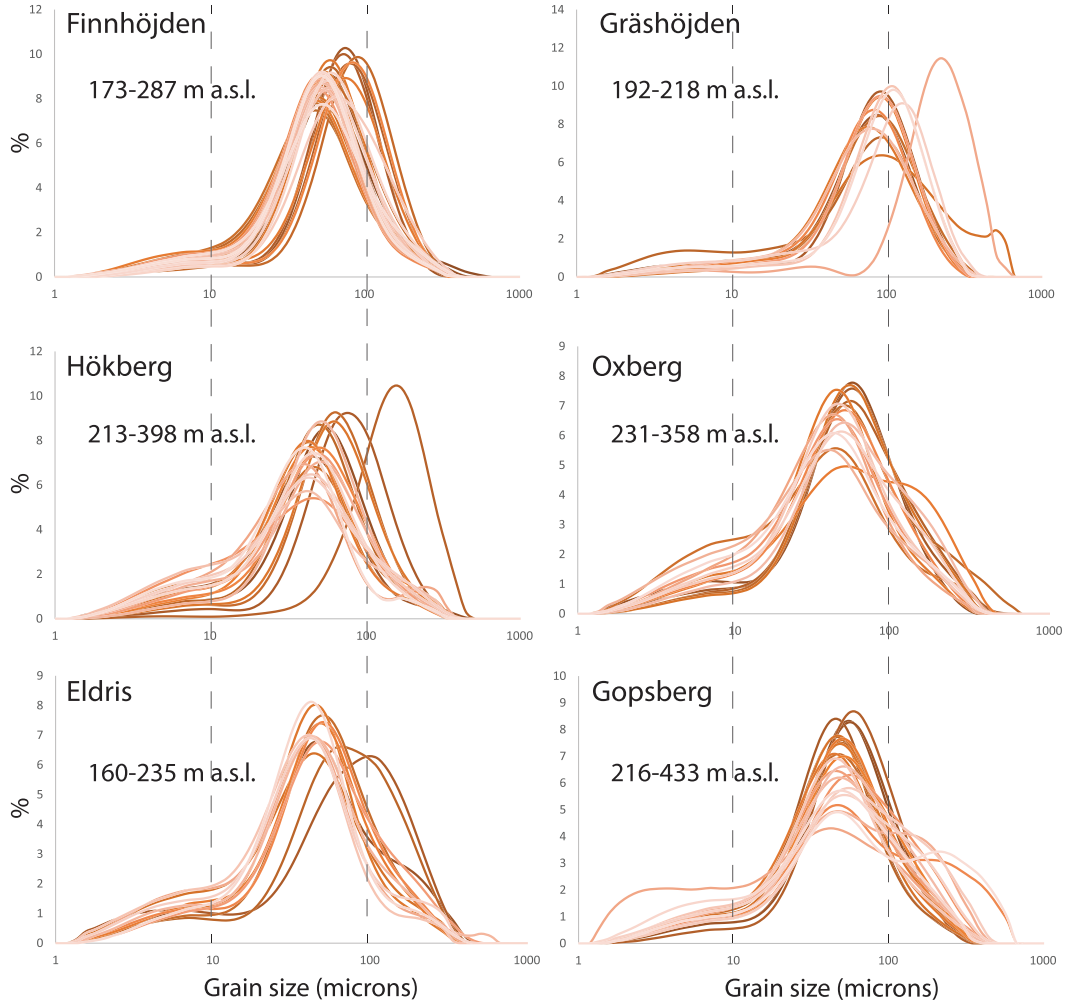

FIGURE 6 Grain size distributions for loess sampling points in Figures 4 and 5 shaded by altitude. Highest points have lighter shades. Range of elevation indicated in plots [Color figure can be viewed at wileyonlinelibrary.com]

lower ground, closer to the modern river valley. Detailed mapping at Hökberg (Figure 5A) reveals spatially more extensive loess deposits lying to the southeast than shown previously by Hjulström et al. (1955). Mapping in adjacent areas (Figures 5B–D) also confirms suggestions by Hjulström et al. (1955) that loess deposits are extensive on higher ground in the surrounding area, southwest of the modern Österdalälven River. Loess deposits are likely more extensive than mapped even here. Notably, loess tends to be found more on the north and east sides of the hills, shows close association with cover sands, and is absent from hills northeast of the modern river valley (Figure 5). Loess thickness varies, with a maximum of 50–60 cm and the majority between 10 and 20 cm thick, similar to Brattforsheden. The thickest deposits at all sites often lie closest to the dunes and cover sands at lower elevations. Further west the loess thickness decreases. The thickest deposits also tend to be coarsest, although the spatial trends in grain size tend to be more variable, especially at Oxberg and Gopsberg (Figure 5). Typical mean grain sizes lie in the medium to coarse silt range, grading into fine sands near the boundary with cover sands. Grain size distributions from mapping samples plotted by altitude and latitude are presented in Figures 6 and 7, respectively. As with Finnhöjden in Brattforsheden, the loess generally becomes finer grained at higher elevations at all sites in the area (Figure 6). Spatial trends by latitude are less clear (Figure 6), with Hökberg and Eldris in the south of the study area showing coarser loess in the north of the areas, while no clear pattern is seen at Oxberg and Gopsberg. The geographic trends by longitude (Figure S1) are also inconsistent, with Hökberg showing coarsening to the west and slight coarsening to the east at other sites.

3.2 | Luminescence dating: luminescence tests

The purity of quartz material was monitored using the OSL IR depletion ratio test (Duller, 2003). After two HF treatments, all samples showed an OSL depletion ratio within 10% of unity, indicating no or insignificant IR-sensitive feldspar contributions to the net OSL decay signal. In order to select the appropriate thermal treatment for the SAR protocol, the D_e dependency on temperature was monitored through preheat plateau and dose recovery preheat plateau tests on samples HB0102 (Hökberg), GH1–30 and GH2–20 (Gräshöjden), which are considered representative for samples and sections. Samples from Gräshöjden are also considered likely to be representative for the FH1 and FH2 sections at Finnhöjden as they are from the same depositional area and share the same source material. Eighteen aliquots per sample were bleached twice inside the reader at room temperature with blue stimulation (200 s each) separated by a pause

10969837, 2022, 14, Downloaded from https://onlinelibrary.wiley.com/doi/10.1002/esp.5456 by CochraneItalia, Wiley Online Library on [19/12/2024]. See the Terms and Conditions (https://onlinelibrary.wiley.com/terms-and-conditions) on Wiley Online Library for rules of use; OA articles are governed by the applicable Creative Commons License

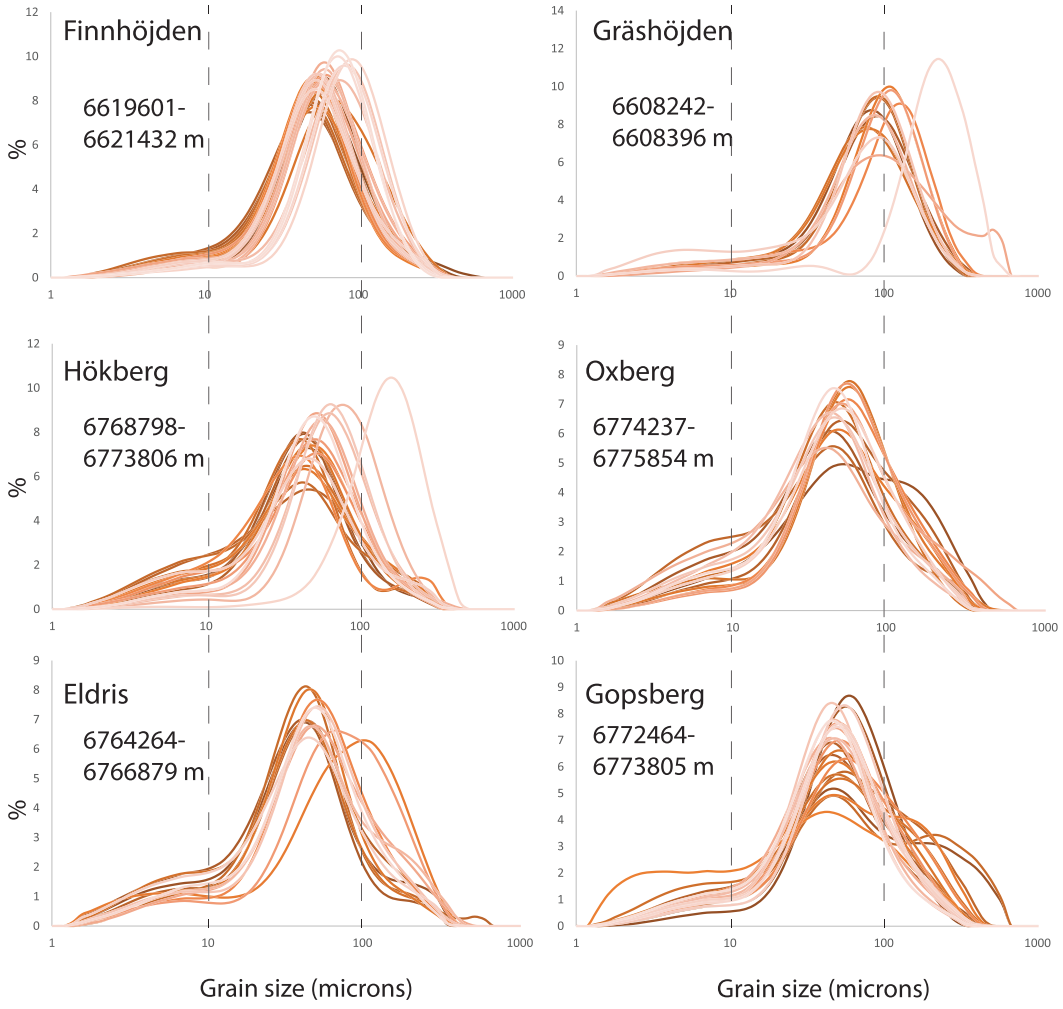

FIGURE 7 Grain size distributions for loess mapping points in Figures 4 and 5 shaded by northing position. Sites further north have lighter shades. Range of northings indicated in plots according to SWEREF 99 grid system (units in metres) [Color figure can be viewed at wileyonlinelibrary.com]

of 10 000 s to allow any photo-transferred charge in the 110°C TL trap to decay. A laboratory-administered dose close to the estimated natural was given to the aliquots and analysed with the SAR protocol at increasing preheat temperatures from 180 to 280°C. The cut heat was kept 20°C less than the respective preheat temperature except for 180°C, for which it was set as the same as the preheat. Figure 8 illustrates that the calculated D_e values (average of 4 aliquots) are independent of preheat temperature and that the SAR protocol is able to accurately recover a known laboratory dose (dose recovery ratio close to unity). The tests also show that the recycling ratio is close to unity, and recuperation is <5% of natural D_e (Figure 8C) for the aliquots measured.

For samples with low values of D_e (<15 Gy), it is essential to limit the thermal transfer contribution during thermal treatment (retrapping of charge during heating) on the natural D_e, which can cause D_e overestimation. The thermal transfer was monitored in the same way as preheat temperature using 24 aliquots of samples HB0103 and GH1–30. Aliquots were bleached inside the reader, and the residuals were measured using the same preheat temperatures as used in the preheat plateau tests. Both samples show <2 Gy of thermally transferred dose at 180–220°C, slightly increasing at higher temperatures (Figure 8D). For both samples the dose transfer is minimal (especially GH1–30), further supporting the reliability of the OSL results. Hence, for all samples, in order to reduce the thermal transfer effect as much as possible, along with fully emptying unstable shallow traps before the natural OSL signal measurement, we set the SAR protocol for D_e determination with a preheat of 220°C (duration 10 s) and a cut heat of 200°C. This combination is considered a good balance for the measurements, since a very high temperature can destabilize deeper traps, leading to an overestimation of D_e, whereas a very low temperature can have the opposite effect. Each SAR cycle was concluded with a high-temperature (280°C) blue-light stimulation for 40 s to avoid recuperation.

Figure 8E shows the sensitivity-corrected dose–response curves and the OSL signal decay curves for sample HB0102. The blue light-stimulated OSL signal decays quickly during the first second of stimulation, indicating that the fast component dominates the signals. This characteristic is observed for all samples analysed here. Given that many sedimentary deposits in Sweden suffer from low quartz brightness, this result is consistent with sample sediments being derived at least in part from much more sensitized Dala sandstone, allowing routine quartz SAR D_e determination (Alexanderson, 2022; Alexanderson & Murray, 2012). Calculated D_e values are well below the saturation limit threshold of 85% of $2D_0$ (Wintle & Murray, 2006). The exception is sample FH1–8 taken at the boundary with underlying moraine and bedrock. Even if this sample exhibits good

10969837, 2022, 14, Downloaded from https://onlinelibrary.wiley.com/doi/10.1002/esp.5456 by CochraneItalia, Wiley Online Library on [19/12/2024]. See the Terms and Conditions (https://onlinelibrary.wiley.com/terms-and-conditions) on Wiley Online Library for rules of use; OA articles are governed by the applicable Creative Commons License

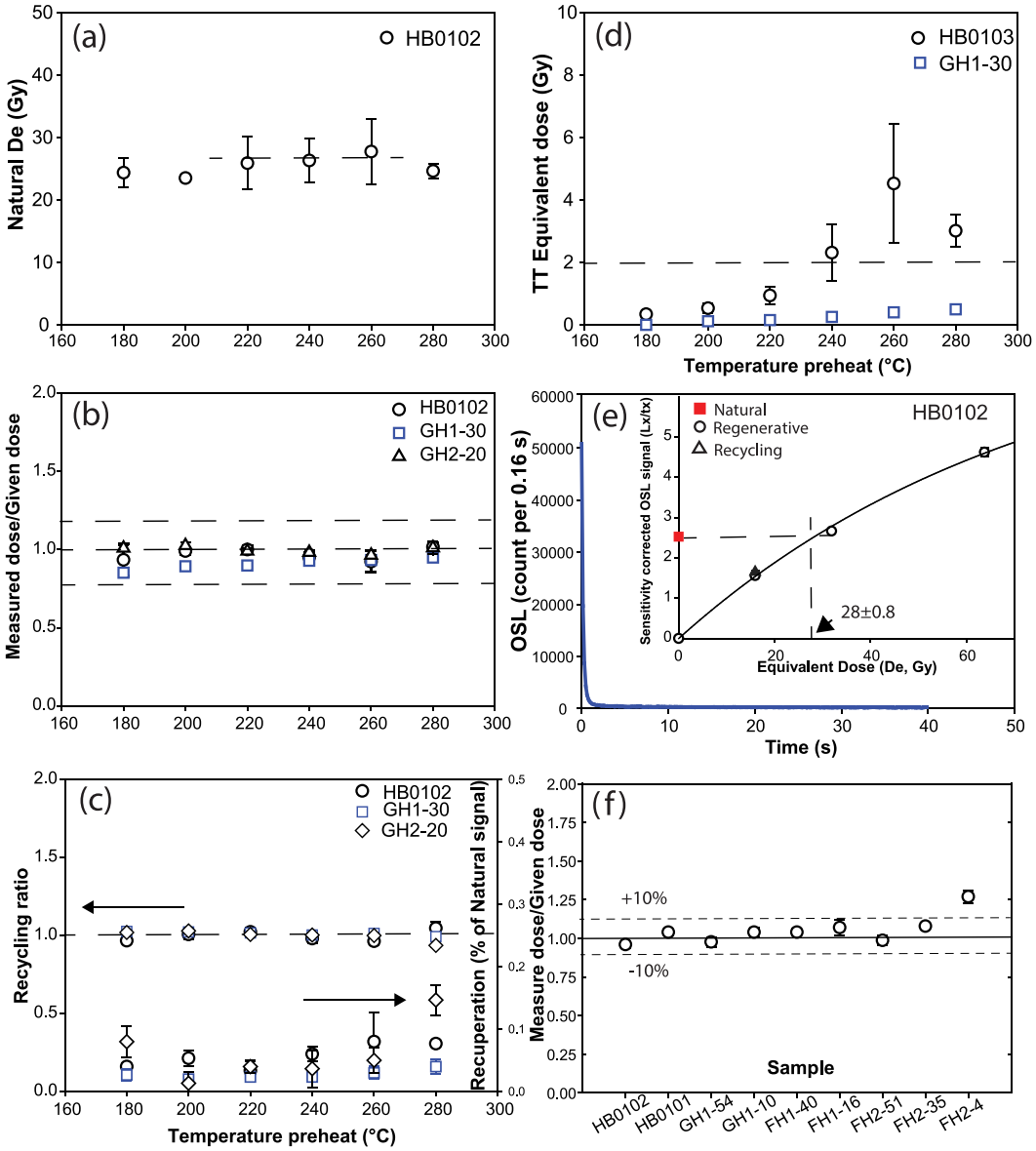

FIGURE 8 (A) Preheat plateau test for sample HB0102. Each data point represents the average of four measurements for each temperature from 180 to 280°C. (B) Dose recovery preheat plateau test performed on samples HB0102, GH1–30 and GH2–20. On the *y*-axis is the range of acceptance for dose recovery ratio (measured dose/given dose) (±10% of unity). (C) Recycling and recuperation measured during dose recovery preheat plateau tests. The dashed line serves as a guide to indicate perfect recycling. (D) Result of thermal transfer (TT) test on samples HB0103 (younger sample of the HB section) and GH1–30 on 24 aliquots bleached inside the reader and luminescence signal measured in the same temperature range as for the preheat plateau tests. (E) OSL fast component-dominated luminescence decay from an aliquot of sample HB0102. Inset shows SAR dose–response growth curve. A repeat point (white circle) and a zero-dose point are also shown. The red square shows the natural signal lx/Tx while the triangle shows the recycling point. (F) Dose recovery test performance on 24 aliquots of different samples. The overdispersion (OD%) of measured recovered dose is used to calculate the intrinsic source of dispersion (see Table 1) [Color figure can be viewed at wileyonlinelibrary.com]

luminescence characteristics, the natural signal is beyond the saturation limits (Table 1).

3.3 | Luminescence dating results

Routine calculation of reliable D_e values requires complete resetting of the luminescence signal prior to burial. For young samples (0–20 ka), fixed thresholds have previously been adopted to determine between well-bleached and partially bleached samples (e.g. overdispersion [OD] < 20%; Arnold & Roberts, 2009). However, despite high values of OD potentially suggesting poor bleaching or post-depositional disturbance of sediments, high scatter in the D_e distribution (OD > 20%) may also arise from a combination of intrinsic (luminescence characteristics, instrument reproducibility) and extrinsic sources (heterogenous external microdosimetry and grain size) (Guérin et al., 2017; Smedley et al., 2020; Thomsen et al., 2016).

Although we expect to see good bleaching of aeolian samples from Sweden (Alexanderson & Murray, 2012), the uncertainty over the genesis of the samples analysed here necessitates a thorough check for evidence of partial bleaching. To evaluate good resetting of the signal prior to burial, the shape of D_e dispersion is analysed using Abanico plots (Dietze et al., 2016) (Figure S2). D_e distribution shapes do not clearly highlight the presence of different clusters of grain D_e

10969837, 2022, 14, Downloaded from https://onlinelibrary.wiley.com/doi/10.1002/esp.5456 by CochraneItalia, Wiley Online Library on [19/12/2024]. See the Terms and Conditions (https://onlinelibrary.wiley.com/terms-and-conditions) on Wiley Online Library for rules of use; OA articles are governed by the applicable Creative Commons License

TABLE 1 Equivalent dose (D_e) results (unweighted mean), W_t (weighted mean) CAM (central dose model) and ADM (average dose model) *sensu* Guérin et al. (2017) in comparison to D_e ratio (obtained from the average of CAM/D_e, ADM/D_e and D_eW_t/D_e ratios). Skew = skewness value, OD = overdispersion expressed as a percentage (%) and source of dispersion (OD_{in} and OD_{ex}) are also shown. *n*/*N* is the number of accepted aliquots/number of measured aliquots

Sample	*n*/*N*	D_e (avg) (Gy)	W_tD_e (Gy)	CAM (Gy)	ADM (Gy)	D_e ratio	Skew	OD (%)	OD_{in} (%)	OD_{ex} (%)
HB0103	23/24	20.4 ± 1.0	20.5 ± 1.0	19.9 ± 1.0		0.98 ± 0.01	−0.1	24		
HB0102	39/41	26.3 ± 1.0	25.6 ± 1.1	25.7 ± 1.0	26.3 ± 1.0	0.99 ± 0.01	0.1	24	10	21
HB0101	39/41	79.6 ± 4.4	81.9 ± 4.6	74.9 ± 4.3	79.6 ± 4.4	0.97 ± 0.03	0.3	35	5	35
GH1–54	37/40	11.8 ± 0.4	11.5 ± 0.4	11.6 ± 0.4	11.8 ± 0.4	0.99 ± 0.01	0.5	20	5	19
GH1–45	27/30	21.2 ± 0.4	21.3 ± 0.4	21.1 ± 0.4		1.00 ± 0.00	0.4	9		
GH1–30	21/24	23.5 ± 0.3	23.5 ± 0.3	23.4 ± 0.3		1.00 ± 0.00	0.4	5		
GH1–20	23/24	24.8 ± 0.5	24.9 ± 0.4	24.7 ± 0.5		1.00 ± 0.00	−0.4	8		
GH1–10	37/41	25.7 ± 0.8	26.5 ± 1.0	25.1 ± 0.8	25.4 ± 0.8	0.99 ± 0.02	0.1	18	8	15
GH240	27/29	23.8 ± 0.4	23.8 ± 0.4	23.7 ± 0.4		1.00 ± 0.00	−0.1	7		
GH220	27/35	23.7 ± 0.4	23.7 ± 0.4	23.6 ± 0.4		1.00 ± 0.00	−0.5	9		
GH20	24/29	26.3 ± 0.5	26.3 ± 0.5	26.2 ± 0.5		1.00 ± 0.00	0.0	10		
FH1–40	39/42	16.8 ± 0.6	16.4 ± 0.6	16.4 ± 0.6	16.8 ± 0.7	0.99 ± 0.01	−0.9	23	7	22
FH1–29	22/24	22.1 ± 0.6	22.3 ± 0.6	21.8 ± 0.6		0.99 ± 0.01	0.0	13		
FH1–16	36/42	87.5 ± 5.0	90.0 ± 4.9	82.1 ± 4.9	86.2 ± 5.4	0.97 ± 0.03	−0.8	35	17	28
FH1–8						0.00 ± 0.00				
FH2–51	34/37	19.3 ± 1.1	20.1 ± 1.1	18.1 ± 1.1	19.2 ± 1.0	0.97 ± 0.03	−0.6	34	5	33
FH2–41	22/24	28.9 ± 1.2	29.2 ± 1.2	28.2 ± 1.2		0.74 ± 0.25	0.2	17		
FH2–35	36/46	75.5 ± 5.1	80.9 ± 5.2	68.6 ± 4.9	74.3 ± 5.2	0.95 ± 0.05	−0.5	41	10	39
FH2–27	26/27	345.9 ± 17.5	355.6 ± 17.0	333.7 ± 17.3		0.98 ± 0.03	0.6	26		
FH2–14	24/29	446.4 ± 20.5	464.7 ± 20.7	431.9 ± 19.7		0.98 ± 0.03	−0.5	21		
FH2–4	30/44	517.2 ± 22.1	536.6 ± 21.9	500.2 ± 22.2	511.3 ± 20.9	0.98 ± 0.02	0.1	23	11	20

values and, in general, distributions are platykurtic and symmetrical (skewness close to 0) with relatively low values of ~20% OD (from 5 to 41%) (Table 1, Figure S2). Higher values of OD were observed for the top and bottom of the sections and particularly close to the base of what was interpreted as loess in the field (Table 2). All sections show general increases in D_e values with depth.

In order to estimate the most appropriate burial dose, the main different central values of the dose distributions (average mean, weighted mean) and dose models CAM (central age model; Galbraith & Roberts, 2012) and ADM (average dose model; Guérin et al., 2017) were calculated (Table 1). The ADM takes into account the intrinsic and extrinsic contribution of scatter in the D_e distribution, giving a better description of D_e heterogeneity (Guérin et al., 2017). The OD source components for representative samples (bottom and top of each section) were calculated, with the exception of section GH2, which shows the lowest values of OD. The intrinsic contributions (OD_{in}) are obtained from the dose recovery experiments (Figure 8F), whereas the extrinsic contribution (OD_{ex}) is quantified by subtracting (in quadrature) the OD_{in} from the total OD (Smedley et al., 2020). The distributions of estimated recovered doses are plotted as red lines in Figure S2, alongside the natural D_e distribution, to evaluate differences in the shape and scatter between natural and administered dose distributions. The shapes of recovered dose distributions are slightly leptokurtic and OD_{in} is considered low (<10%), apart from in sample FH2–35, which shows the highest value (17%) (Table 1). Hence, most of the source of the scattering in the D_e distributions is ascribable to extrinsic factors. However, considering the relatively low values of OD_{ex}, much of the scatter in D_e likely mostly arises from variability in microdosimetry (beta-dose internal variability due to K-feldspar hotspots) and/or grain size rather than poor bleaching or post-depositional disturbance (Sechi et al., 2020; Smedley et al., 2020; Stevens et al., 2020; Thomsen et al., 2016).

Comparison of empirical mean (unweighted and weighted) D_e with the dose models (CAM, ADM) shows great consistency within errors (2σ), with D_e ratios on average close to unity (Table 1). The general agreement of all estimated values of D_e for each sample, the generally symmetrical D_e distributions and the OD values for most of the samples suggest that the sediment was well bleached prior to deposition. The final estimated burial palaeodose appears well constrained by the different methods, and the low scatter in D_e values does not influence the final burial age estimation. As such, there is no need to apply age modelling to distinguish between different populations and to determine final burial ages (Guérin et al., 2017). Nevertheless, to take into account unrevealed additional sources of scatter in the D_e as much as possible, we decided to use the CAM model for age estimation (*sensu* Guérin et al., 2017). However, the possibility of poor bleaching or post-depositional disturbance in some samples cannot be entirely excluded based on the dating and proxy results, as discussed below.

The full luminescence dating results used in age determination are presented in Table 2. Good performance of recycling ratio and recuperation for all samples was observed. Note that sampling for luminescence at Brattforsheden was undertaken during spring snowmelt and natural sampled water contents at Gräshöjden were strongly

10969837, 2022, 14, Downloaded from https://onlinelibrary.wiley.com/doi/10.1002/esp.5456 by CochraneItalia, Wiley Online Library on [19/12/2024]. See the Terms and Conditions (https://onlinelibrary.wiley.com/terms-and-conditions) on Wiley Online Library for rules of use; OA articles are governed by the applicable Creative Commons License

TABLE 2 WC = water content (±20%); see text for details. DR = dose rate. CAM D_e = equivalent dose derived from the CAM age model (see text). All radioisotopes are presented with ±5% uncertainty. Cosmic dose rate is calculated based on Prescott and Hutton (1994). Uncertainty in ages contains both random and systematic components

Sample	Depth (cm)	WC (%)	U (ppm)	Th (ppm)	K (%)	CAM D_e (Gy)	Cosmic (Gy ka^{-1})	Total DR (Gy ka^{-1})	Age (ka)
HB0103	9.0	20.0	1.2 ± 0.01	2.3 ± 0.01	1.70 ± 0.1	19.9 ± 1.00	0.20 ± 0.01	1.94 ± 0.08	10.30 ± 0.70
HB0102	17.0	20.0	1.2 ± 0.01	2.6 ± 0.01	2.00 ± 0.1	25.7 ± 1.00	0.20 ± 0.01	2.18 ± 0.09	11.80 ± 0.70
HB0101	27.0	17.0	1.6 ± 0.01	3.9 ± 0.01	2.30 ± 0.1	74.9 ± 4.30	0.20 ± 0.01	2.63 ± 0.10	28.40 ± 2.00
GH1–54	6.0	16.0	1.6 ± 0.01	2.2 ± 0.01	2.20 ± 0.1	11.6 ± 0.40	0.20 ± 0.01	2.48 ± 0.10	4.70 ± 0.20
GH1–45	15.0	20.0	2.5 ± 0.01	6.0 ± 0.01	2.50 ± 0.1	21.1 ± 0.40	0.20 ± 0.01	3.04 ± 0.11	6.90 ± 0.30
GH1–30	30.0	18.0	2.3 ± 0.01	5.6 ± 0.01	2.80 ± 0.1	23.4 ± 0.30	0.19 ± 0.01	3.23 ± 0.13	7.30 ± 0.30
GH1–20	40.0	20.0	2.3 ± 0.01	5.7 ± 0.01	3.00 ± 0.1	24.7 ± 0.50	0.19 ± 0.01	3.37 ± 0.14	7.30 ± 0.30
GH1–10	50.0	18.0	2.2 ± 0.01	5.7 ± 0.01	2.70 ± 0.1	25.1 ± 0.80	0.19 ± 0.01	3.16 ± 0.12	7.90 ± 0.40
GH2–40	11.0	22.0	3.8 ± 0.01	8.0 ± 0.01	2.50 ± 0.1	23.7 ± 0.40	0.20 ± 0.01	3.34 ± 0.12	7.10 ± 0.30
GH2–20	31.0	24.0	4.8 ± 0.01	12.9 ± 0.01	2.70 ± 0.1	23.6 ± 0.40	0.19 ± 0.01	3.88 ± 0.14	6.10 ± 0.20
GH2–0	51.0	20.0	4.5 ± 0.01	7.8 ± 0.01	2.50 ± 0.1	26.2 ± 0.50	0.19 ± 0.01	3.50 ± 0.12	7.50 ± 0.30
FH1–40	10.0	17.0	1.8 ± 0.01	3.0 ± 0.01	2.50 ± 0.1	16.4 ± 0.60	0.20 ± 0.01	2.80 ± 0.11	5.80 ± 0.30
FH1–29	21.0	16.0	2.0 ± 0.01	3.8 ± 0.01	2.60 ± 0.1	21.8 ± 0.60	0.20 ± 0.01	3.00 ± 0.12	7.30 ± 0.40
FH1–16	34.0	20.0	2.3 ± 0.01	5.8 ± 0.01	2.60 ± 0.1	82.1 ± 4.90	0.20 ± 0.01	3.05 ± 0.12	26.90 ± 1.90
FH1–8 42	0.0	22.0	2.0 ± 0.01	5.4 ± 0.01	2.50 ± 0.1	Sat	0.19 ± 0.01	2.86 ± 0.11	0.00 ± 0.00
FH2–51	5.0	10.0	1.8 ± 0.01	3.2 ± 0.01	2.60 ± 0.1	18.1 ± 1.10	0.20 ± 0.01	3.10 ± 0.11	5.80 ± 0.40
FH2–41	15.0	12.0	2.4 ± 0.01	5.9 ± 0.01	2.50 ± 0.1	28.2 ± 1.20	0.20 ± 0.01	3.24 ± 0.11	8.70 ± 0.50
FH2–35	21.0	16.0	2.3 ± 0.01	5.7 ± 0.01	2.60 ± 0.1	68.6 ± 4.90	0.20 ± 0.01	3.16 ± 0.12	21.70 ± 1.70
FH2–27	29.0	21.0	2.1 ± 0.01	5.5 ± 0.01	2.90 ± 0.1	333.7 ± 17.30	0.20 ± 0.01	3.20 ± 0.13	104.40 ± 6.90
FH2–14	42.0	23.0	1.7 ± 0.01	4.7 ± 0.01	2.60 ± 0.1	431.9 ± 19.70	0.19 ± 0.01	2.80 ± 0.12	154.10 ± 9.60
FH2–4	52.0	20.0	2.0 ± 0.01	5.9 ± 0.01	2.90 ± 0.1	500.2 ± 22.20	0.19 ± 0.01	3.22 ± 0.13	155.30 ± 9.30

affected by water pooling from this melt. In contrast, sampling in Hökberg was conducted in autumn. Measured *in-situ* water contents for Gräshöjden samples were at saturation, while *in-situ* measured water content from samples taken from Finnhöjden and Hökberg was 15–20% of the initial sample weight (Table 2). These latter estimates were considered more reliable estimates of burial water content for the samples than the estimates at Gräshöjden. Thus, to estimate a more realistic burial water content for the Gräshöjden samples, values 50% of the measured saturation level were chosen (Table 2). This approach yielded percentage water content estimates in line with *in-situ* values at Hökberg and Finnhöjden. Nonetheless, given the significant uncertainties in this approach and the uncertainty over how water contents may have fluctuated since burial, a 20% error uncertainty is assigned to these values.

3.4 | Stratigraphy, luminescence ages and sediment analyses

The pit at Hökberg (HB0101; N61.07°, E14.31°) is shown in Figure 9 and a photo of the section in Figure S3, alongside examples from Finnhöjden and Gräshöjden. Porous, massive, open-structured, non-calcareous silty sediments were logged to a depth of 33 cm at the section, with the upper 8 cm covered by roots and moss. Silt deposits were gravel-free and divided into an ash-coloured upper unit and a red, iron-stained lower unit, indicating podsolization (E and B horizons, respectively). The B horizon was mottled and contained humic streaks. At the base of the section the orange silts graded to a cobble clast-rich silt, mapped as till by the SGU. OSL ages from three samples are in stratigraphic order and range from c. 10 to 28 ka, with a large jump in age in the bottom-most sample taken in the orange unit (Figure 9). Sand content and grain size generally decrease upwards from the orange to the ash-coloured unit, with coarse silt modes throughout, while χlf and χfn show an inverse relationship. Al/Fe, CIA and Rb/Sr (weathering indices) increase up-section while Ti/Zr (provenance and grain size indicator) shows a spike and higher values generally at the base of the profile (Figure 9).

At Finnhöjden and Gräshöjden, two sections in each area were sampled (Figure S3). At Finnhöjden a pit section (FH1; N59.72°, E13.84°) and roadside exposure (FH2; N59.72°, E13.84°) were sampled (Figure 10). According to SGU mapping, both sections are on sandy till. The sections dug were >50 cm deep and are overlain by c. 5 cm of leaf and moss litter. The lowermost unit at both sites was sandier in texture, containing sporadic larger gravel-sized clasts, and was underlain by large boulder or cobble clasts. Overlying this unit was a sequence of progressively darkening orange, open-structured, massive, non-calcareous silts, with sporadic, isolated gravel clasts from the base up to 18–20 cm depth, coinciding broadly with the colour boundary separating the dark orange B horizon from underlying lighter horizons. Overlying this horizon was an ash-coloured horizon (E horizon of podsol). The OSL ages from the two sections show similar patterns, with the uppermost ash-coloured silt and first dark orange horizon showing ages ranging from c. 6 to 9 ka (Figure 10). Below this point, the ages jump rapidly up to c. 22 ka to beyond

10969837, 2022, 14, Downloaded from https://onlinelibrary.wiley.com/doi/10.1002/esp.5456 by CochraneItalia, Wiley Online Library on [19/12/2024]. See the Terms and Conditions (https://onlinelibrary.wiley.com/terms-and-conditions) on Wiley Online Library for rules of use; OA articles are governed by the applicable Creative Commons License

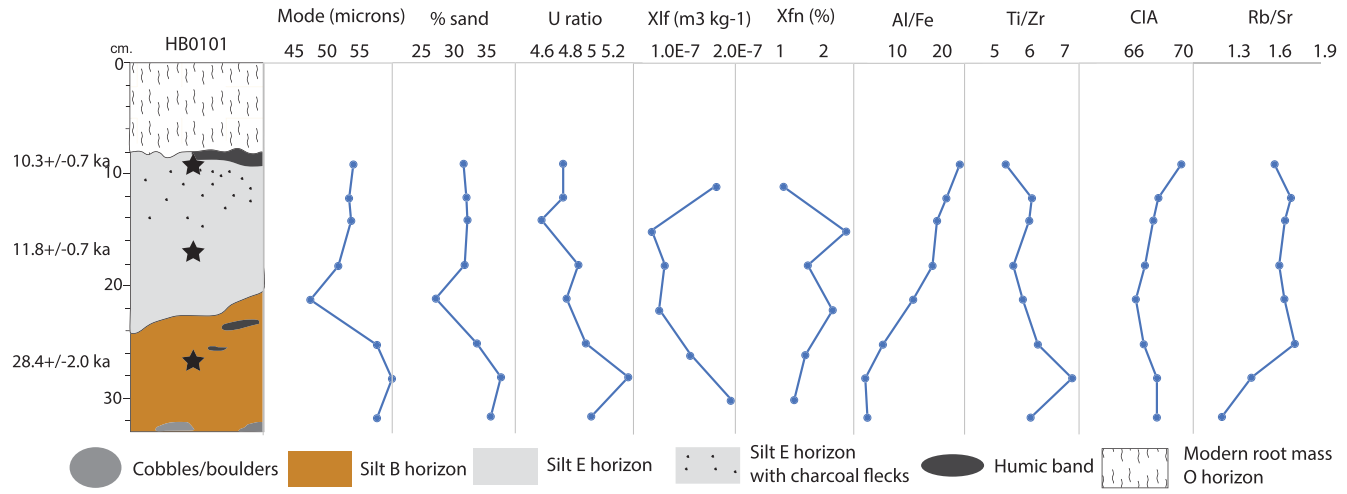

FIGURE 9 Stratigraphic log, OSL dating results, grain size analysis indices, magnetic susceptibility parameters and geochemical indices plotted by depth at HB0101 (Hökberg). Note that on the stratigraphic log, stars show the position of the luminescence samples [Color figure can be viewed at wileyonlinelibrary.com]

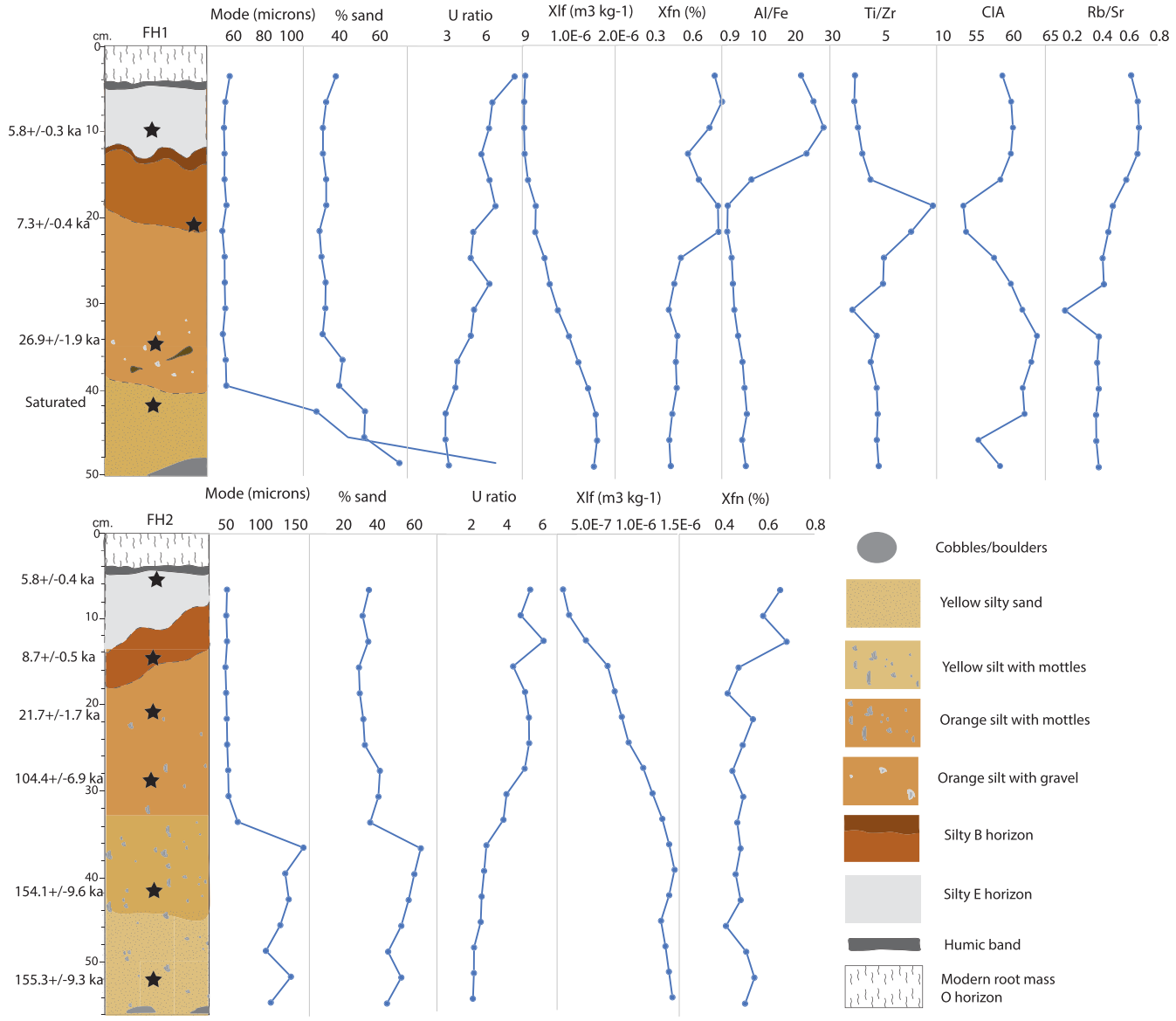

FIGURE 10 Stratigraphic logs, OSL dating results, grain size analysis indices, magnetic susceptibility parameters and geochemical indices plotted by depth at FH1 and FH2 sites (Finnhöjden). Note that on the stratigraphic logs, stars show the position of the luminescence samples [Color figure can be viewed at wileyonlinelibrary.com]

10969837, 2022, 14, Downloaded from https://onlinelibrary.wiley.com/doi/10.1002/esp.5456 by CochraneItalia, Wiley Online Library on [19/12/2024]. See the Terms and Conditions (https://onlinelibrary.wiley.com/terms-and-conditions) on Wiley Online Library for rules of use; OA articles are governed by the applicable Creative Commons License

saturation limits, although still maintaining stratigraphic order by age. Sand content and modal grain size show a major increase in the bottom sandy unit at FH1 and the bottom two units at FH2, above which modes are in the coarse silt range and c. 30% sand (Figure 10). Notably, the U ratio shows a different trend, with tendencies to coarser silt dominating higher up the sections. This trend implies that the changes at the base of the section are due to an increase of sand content only, and not a general coarsening of the silt fraction. The χlf and χfn indices show an inverse relationship, with higher χlf at the base of the sections. Geochemical indices from FH1 show abrupt shifts in Al/Fe, CIA and Ti/Zr in the upper 20 cm, with some variability in Ti/Zr below this level (Figure 10).

At Gräshöjden a roadside exposure (GH1; N59.608304°, E13.956998°) and pit section (GH2; N59.608491°, E13.957109°) lying c. 200 m west of a large N–S oriented dune ridge were sampled (Figure 11). According to SGU mapping, both sections are underlain by sandy till. The sections dug reached 60 cm deep and were overlain c. 5 cm of modern leaf and moss litter. Section GH1 was to a large

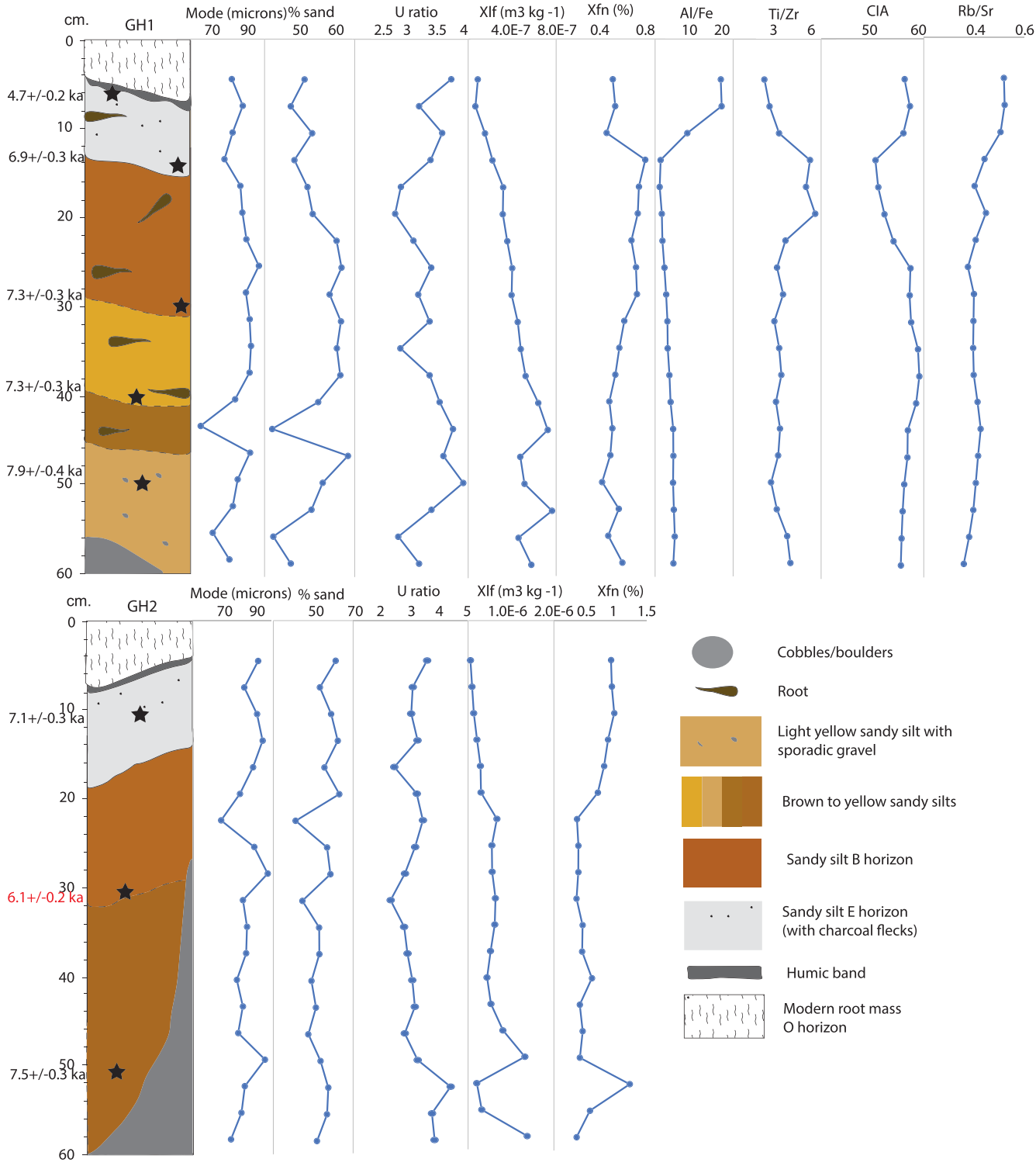

FIGURE 11 Stratigraphic logs, OSL dating results, grain size analysis indices, magnetic susceptibility parameters and geochemical indices plotted by depth at GH1 and GH2 sites (Gräshöjden). Note that on the stratigraphic logs, stars show the position of the luminescence samples [Color figure can be viewed at wileyonlinelibrary.com]

10969837, 2022, 14, Downloaded from https://onlinelibrary.wiley.com/doi/10.1002/esp.5456 by CochraneItalia, Wiley Online Library on [19/12/2024]. See the Terms and Conditions (https://onlinelibrary.wiley.com/terms-and-conditions) on Wiley Online Library for rules of use; OA articles are governed by the applicable Creative Commons License

extent affected by large roots, but both sections were mostly free of gravel and are dominated by massive, silty/sandy horizons of varying colour, although at GH1 the lowermost unit, below c. 46 cm, contained sporadic gravel clasts. As with other sites, the upper silt–sand horizon was ash coloured with variously light to dark and yellow orange horizons exposed below. Colour variation by depth is different between sites and is complicated by different degrees of water saturation (Figure 11). OSL ages from the two sections show similar patterns with ages ranging from c. 5 to 8 ka, and in stratigraphic order except for a single age from GH2 (red in Figure 11). No pre-Holocene ages occur at these sections, in contrast to the FH and HB sections. Both sections are much sandier than at Finnhöjden and Hökberg, with sand contents >50% and modes around the fine sand range. No clear trends with depth occur in the grain size indices but as with other sites, the χlf and χfn indices show an inverse relationship, with higher χlf at the base of the sections. Geochemical indices from GH1 show abrupt shifts in Al/Fe in the top 14 cm, gradual increases in Rb/Sr from c. 22 cm, and changes in CIA and Ti/Zr between c. 14 and 25 cm depth, coinciding with the upper part of the uppermost orange (B) horizon (Figure 11).

In order to examine grain size changes by depth in more detail, grain size distributions for each sample at all sites are shown in Figure 12, compared to typical loess from NW Europe from the Pegwell Bay site in SE England (Stevens et al., 2020). Very little difference down-section is seen at HB0101, and the distributions are typical for loess, characterized by coarse silt modes, an absence of coarse or medium sand, and by a fine tail in the fine silt and clay fraction. This tail is relatively less significant than at Pegwell Bay. GH1 and GH2 also generally show limited textural variability with depth. Overall, distributions are similar to those seen at HB0101 but the distributions are coarser (with modes in the fine sand fraction) and the fine tail of the distribution extended. By contrast, there is great variability in grain size distributions at FH1 and FH2. The distribution shapes are similar to those at Pegwell Bay as well as HB0101, GH1 and GH2, and show typical loess characteristics, near identical to those at HB0101. These distributions are from samples higher in the profile, while stratigraphically deeper samples show quite different characteristics. Notably, these deeper samples tend to show much coarser modes (in the fine and medium sand fraction), a more even spread of grain sizes, poorer sorting and a much larger proportion of medium and even coarse sand (Figure 12).

3.5 | SEM analyses

Ten samples from Finnhöjden (FH1, FH2), Gräshöjden (GH1, GH2) and Hökberg (HB01) loess sections were studied under SEM. The majority of scanned grains in all samples were silt-sized particles (<63 μm). A smaller percentage of grains (<20%) were sand-sized (>63 μm), consisting of dominantly fine-grained sand, and these grains

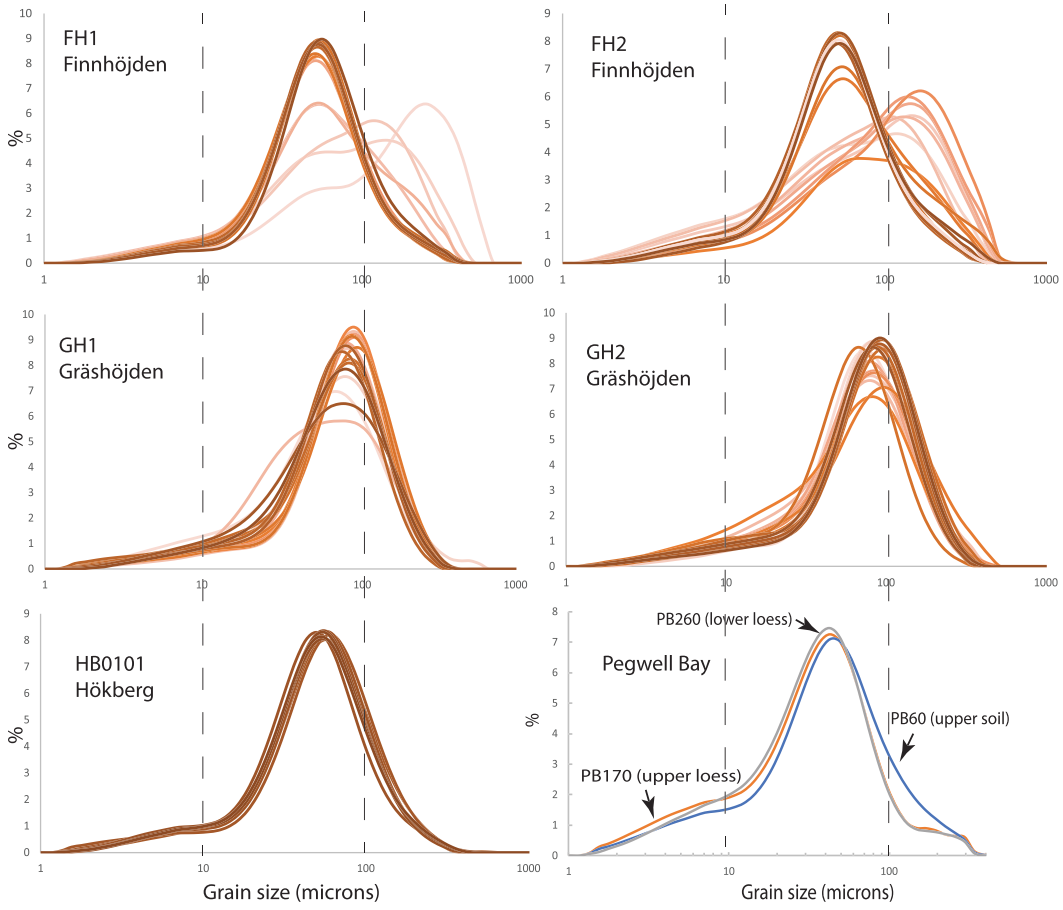

FIGURE 12 Grain size distributions for every sample from each site shaded by depth (lighter colours indicate deeper samples). Distributions from the sites here are compared to three typical samples from the loess and Holocene soil from the Pegwell Bay site (PB) in southeast England (Stevens et al., 2020) [Color figure can be viewed at wileyonlinelibrary.com]

10969837, 2022, 14, Downloaded from https://onlinelibrary.wiley.com/doi/10.1002/esp.5456 by CochraneItalia, Wiley Online Library on [19/12/2024]. See the Terms and Conditions (https://onlinelibrary.wiley.com/terms-and-conditions) on Wiley Online Library for rules of use; OA articles are governed by the applicable Creative Commons License

were found mostly in GH1 54 and HB0103 samples. Angular grains dominate in all of the analysed samples, comprising almost 70% of the total number of grains. Around 20% of the grains are very angular or sub-angular. Sub-rounded grains make up almost 10% of all grains. Rounded and well-rounded grains were not detected in the samples and the majority of the grains display high relief, with <20% displaying low relief. Surface textures generally cover smaller parts of the grains with dimensions of 5–10 μm, but in some samples they make up half of the grain or cover the entire grain (Figures 13B, H, I and K). Conchoidal fractures (Figure 13) are present in >40% of the samples and almost 30% of the grains have visible sets of subparallel linear fractures. These two surface textures are the most common features of the analysed grains. Parallel and radial steps together with straight grooves are also present on a small percentage of the grains (<10%).

4 | DISCUSSION

4.1 | Luminescence ages in thin Swedish loess deposits

The quartz OSL signal here appears fast component-dominated and reproducible, and the chosen SAR protocol satisfies internal tests as to its reliability. This finding is consistent with Alexanderson and Murray (2012) and Alexanderson (2022), who found similar luminescence characteristics for sediments likely derived from the Dala Sandstone in Sweden. However, we note that luminescence dating of thin loess deposits as found at the studied sites may be especially affected by pedoturbation and sediment mixing (Bateman et al., 2007; Schaetzl & Luehmann, 2013; Schaetzl et al., 2014). In

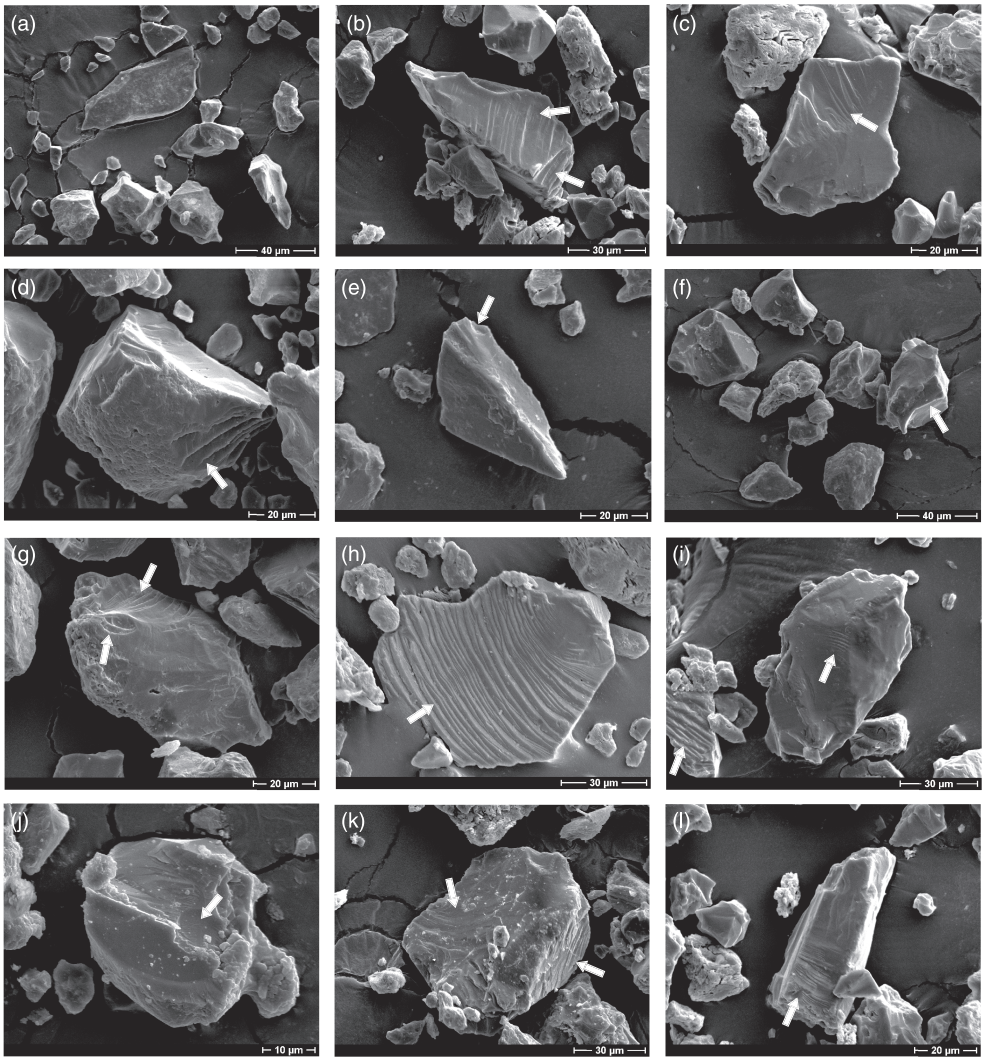

FIGURE 13 SEM images of quartz grains. (A) Sample FH1 3–6: angular and very angular, sharp-edged grains. (B) Sample FH1 45–48: crushed, angular, sharp-edged grain with relatively low relief and subparallel linear fractures marked with arrows. (C) Sample FH1 45–48: angular grain with subparallel linear fractures on the upper part of the grain and conchoidal fracture on the lower part. (D) Sample FH2 15–18: sub-angular grain with fracture face at the top of the grain and radial steps marked with an arrow. (E) Sample FH2 30–33: angular grain with sharper edges and conchoidal fracture marked with an arrow. (F) FH2 30–33: angular and sub-angular grains with fracture faces and conchoidal fracture marked with an arrow. (G) Sample GH1 10: well-crushed, sub-angular grain with rounded edges on the left side and conchoidal fractures marked with arrows. (H) Sample GH1 30: sub-rounded grain with conchoidal fractures that cover almost the entire surface. (I) Sample GH1 54: two grains. Smaller, left-hand-side grain with surface completely covered with deep, linear grooves. Bigger grain with fracture surfaces and subparallel linear fractures (arrows). (J) Sample HB0101: sub-rounded grain with conchoidal fracture and subparallel linear fractures within; marked with an arrow. (K) Sample HB0101: sub-rounded grain with conchoidal fracture on the left side and subparallel fractures on the right side; marked with arrows. (L) Sample HB0103: angular, elongated grain with fracture surfaces and linear steps marked with an arrow

10969837, 2022, 14, Downloaded from https://onlinelibrary.wiley.com/doi/10.1002/esp.5456 by CochraneItalia, Wiley Online Library on [19/12/2024]. See the Terms and Conditions (https://onlinelibrary.wiley.com/terms-and-conditions) on Wiley Online Library for rules of use; OA articles are governed by the applicable Creative Commons License

cases where soil formation causes mixing, this would potentially yield greater dose variability as well as ages younger than loess deposition, if grains were reset through light exposure. For basal parts of loess sequences, mixing processes with underlying sediments may also lead to depositional age overestimates.

A number of luminescence ages from lower parts of the sections at Finnhöjden and Hökberg suggest pre-deglacial ages (27–155 ka; Table 2), which seem implausible given the last glacial ice sheet coverage in the study region (Stroeven et al., 2016). Notably, luminescence aliquot D_e distributions do not clearly highlight the presence of different families of grain D_e values, as might be expected if loess deposits were mixed with underlying older sediment. Furthermore, general agreement of all estimated values of D_e for each sample, the generally symmetrical D_e distributions and the low OD values for most of the samples together suggest that the material was well bleached prior to deposition. OD calculations generally show relatively low values (Table 1, Figure S2), consistent with aeolian transport. However, higher values of OD were observed for the bottom of the sections, particularly close to the base of what was interpreted as loess in the field (Table 2), and may point to mixing with underlying till material in the lower part of the loess units. Another possibility is that the underlying non-loess material is well bleached, although the last glacial ages of some of the samples argue against this. Overall, then, it is noteworthy that if pre-deglaciation ages are a function of mixing with underlying tills, this mixing is not revealed in the equivalent dose distribution. We base our analysis of aliquot dose distribution on 24–48 aliquots, which ought to be sufficient for the identification of mixing (Fuchs et al., 2007). However, more detailed small aliquot or single-grain analyses, potentially on multiple grain sizes, may be required to fully evaluate this possibility.

In the younger, Holocene-age samples there is no evidence for partial bleaching and aliquot D_e distributions do not show skew, high overdispersion or multiple aliquot populations (Figure S2, Table 1). In addition, the consistency of ages with depth at the sites suggests that the ages can be considered reliable estimates of the timing of sediment deposition. Scatter of ages is a defining characteristic in thin loess deposits affected by soil formation (Bateman et al., 2007; Stevens et al., 2007). Furthermore, dose rates and water contents are relatively consistent by depth within sites (Table 2). Overall, then, while luminescence ages taken from thin loess may be more likely to be affected by soil formation and sediment mixing processes, there is no clear evidence from the luminescence analysis to suggest these processes occurred. Rather, the luminescence analysis suggests that the post-glacial OSL ages derived from the silty samples accurately reflect the timing of deposition and burial at the sites (Table 2, Figures 9–11). However, given the apparent symmetrical, well-bleached dose distributions in presumably mixed basal sediments at Finnhöjden and Hökberg, analysis of small aliquot or single-grain dose distributions might test this possibility more fully.

4.2 | Are the silt deposits wind-blown loess?

The grain size distributions for loess deposits in the mapped areas are consistent with loess deposits generally, although at Gräshöjden the distributions exhibit fine-sand modes (Figure 7). Furthermore, as previously noted (e.g. Hjulström et al., 1955; Hörner, 1927), the distribution, grain size and thickness variation of the silt material strongly indicate deposition by wind (Figures 2–5). The deposits cover hill tops, above the highest last deglacial glacial shoreline, blanket underlying terrain and thin away from aeolian sand areas. The general lack of gravel and coarser sand fractions in the sediments also supports an aeolian origin.

The complex processes of producing and transporting silt and sand particles to form loess can be investigated with SEM images, which display the shape of quartz grains and surface microtextures (Trewin, 1988). Some surface textures are dominant in the samples analysed here and are summarized below. Conchoidal fractures (Figure 13), which are the most common features in our samples, are the product of both glacial and aeolian transport of silt and sand (Strand & Immonen, 2010). Almost 30% of the grains have visible sets of subparallel linear fractures (Figure 13), which indicate the process of glacial abrasion of grains under the pressure of ice (Strand & Immonen, 2010). This finding is consistent with derivation of the loess from aeolian reworking of till or glaciofluvial sediment.

We have also detected surface features consistent with glacial transport that are present only in a small number of quartz grains. Parallel and radial steps, observed on a quartz grain from sample FH2 15–18 (Figure 13D), are a product of glacial grinding and these features are common for grains from till. Straight grooves detected in the GH1 54 sample (Figure 13I) also indicate a glacial origin. This texture is produced through a large applied force between grains which scour others of equal or less hardness (Mahaney, 2002). In contrast, V-shaped percussion marks which are a result of bouncing and collision between grains in the process of extended aeolian transport and saltation, and which often can be detected on grains from Pannonian loess deposits (Banak et al., 2013), are not clearly visible on the surface of the analysed grains.

Overall, based on the shape, relief, roundedness and/or angularity and surface microtextures of the silt and sand-sized quartz grains, we conclude that all sites show evidence of sub-glacial production for most of the grains, consistent with the likely source of the material under the last glacial Fennoscandian Ice Sheet. Furthermore, the grains generally show sharp edges, dominantly angular morphology, high relief and conchoidal fractures, which are all common characteristics of aeolian silt and sand-sized particles (Wright, 2007). These observations are consistent with the sediments generally being loess, reworked from the original glacial sediment. However, as V-shaped percussion marks are absent, this transport cannot have been by extended saltation or high-energy glaciofluvial transport. This observation perhaps implies sourcing of the loess sediments directly from tills or from material that has only been transported for a short distance by glaciofluvial processes, rather than far-travelled glaciofluvial sediments or reworked material from the dunes themselves (e.g. Schaetzl et al., 2021).

The dominantly post-glacial ages for much of the material deemed loess here (Table 2) also reinforces the aeolian interpretation. Thus, we conclude that these deposits are loess, and our new mapping of thinner deposits extends the area of known deposits in both Brattforsheden and around Bonäsheden. It is quite likely that the coverage of loess deposits in these areas is even more extensive, and given that there are some reports of further possible loess deposits in other areas of Sweden (Agrell & Hultman, 1971), Norway (Klemsdal, 1969) and Finland (Okko, 1957), we propose that

10969837, 2022, 14, Downloaded from https://onlinelibrary.wiley.com/doi/10.1002/esp.5456 by CochraneItalia, Wiley Online Library on [19/12/2024]. See the Terms and Conditions (https://onlinelibrary.wiley.com/terms-and-conditions) on Wiley Online Library for rules of use; OA articles are governed by the applicable Creative Commons License

windblown dust deposits may be more extensive than previously thought in Fennoscandia.

However, the lower parts of sections at Finnhöjden and Hökberg show characteristics indicative of other sediment types or extensive reworking/mixing of the loess (Figures 6, 7, 9 and 10). Notably, grain size distributions show bimodal or sand-sized modes towards the base of the sections (Figure 12), while OSL ages are far older than the last deglaciation (Figures 9 and 10). By contrast, the sections at Gräshöjden do not show such changes, and luminescence ages constrain the section to the Holocene (Figures 11 and 12). One explanation for the higher sand contents at the base of Finnhöjden and Hökberg sections may be saltating sand grains during early phases of loess deposition (Luehmann et al., 2016). However, given that the underlying sediments at the sites are described as tills and the luminescence ages seem likely to be overestimates, we suggest that in some of the sections till has been reworked or mixed into the overlying loess, either syn- or post-depositionally, as discussed below.

At Hökberg, few proxy record trends with age/depth can be seen that might point to this reworking, due to the very thin nature of the deposit and rapid nature of loess deposition (Figure 9). At Finnhöjden, only the upper parts of the two sections are likely unmixed loess and these deposits show a slight coarsening of the silt fraction up-section (U ratio), along with increasing χfh and decreasing χlf (Figure 10). By contrast, below 30–40 cm there is an abrupt coarsening of the sediment, due to increased sand content (U ratio is not affected), which is consistent with mixing with underlying sandy till. A similar trend in magnetic susceptibility to the upper loess parts of Finnhöjden is also seen at the sites in Gräshöjden (Figure 11), over a greater depth and longer time range. The inverse relationship between χfn and χlf may imply that the wind vigour model controls the magnetic susceptibility signal at the sites, although it may be driven by increased physical weathering in the loess up-section (Bradák et al., 2021), which would be consistent with observed podsolization. Changes in geochemical proxies at Gräshöjden are also consistent with podsol development in the loess, with changing CIA and Al/Fe ratio at the boundary between the E and B horizon, with greater silicate weathering in the upper horizon. Furthermore, SEM analyses show that sample GH1 10 grains are not weathered as much, and have fewer adhering particles than GH1 30 or GH1 54 from the upper part of the section. This observation is also consistent with the greater chemical weathering shown in the upper part of the sequence during the Holocene.

In any case, we conclude that the basal parts of Swedish loess deposits are probably mixed with underlying sediments. This mixing is hard to recognize, except from grain size distribution data and the older than expected luminescence ages. However, we cannot completely exclude that some of the older ages reflect loess remnants that survived the last glacial maximum glaciation, even if this possibility seems highly unlikely. Setting the boundary between the loess and the loess mixed with till at Hökberg and Finnhöjden is not straightforward, as SEM evidence and many of the mineral magnetic and geochemical properties do not show obvious changes. While at Finnhöjden there are clear changes in grain size and stratigraphy around 39 cm (FH1) and 33 cm (FH2), the luminescence ages appear to overestimate probable depositional ages for loess at least from 34 and 21 cm depths, respectively (Figure 10). At Hökberg, no clear changes in stratigraphy or proxies are seen, despite the older luminescence age from the lower part of the section (Figure 9).

The processes that mixed the loess with underlying material at Hökberg and Finnhöjden are unclear at present. Luehmann et al. (2013) argued that pedoturbation mixed underlying sandy till material into the basal parts of thin (<70 cm) locally sourced loess on the Upper Peninsula of Michigan, leading to these basal loesses showing bimodal (sand and silt mode) distributions. Furthermore, Schaetzl and Luehmann (2013) examined relatively coarse basal zones in thin loess deposits from NE Wisconsin and the Upper Peninsula of Michigan and showed secondary modes appearing in the fine or medium sand fraction. They suggested mixing during deposition or by post-depositional pedoturbation and showed these processes occurring as far as 50 cm up from contact with underlying sediments. These observations are strikingly similar to those from our Swedish samples. Furthermore, the geomorphic situation, sources and age of these continental US deposits are also very similar to those of central Sweden. Alternatively, Luehmann et al. (2016) suggest that mixed sand and loess in the lower parts of soils on outwash plains in Michigan may be formed from co-deposition of saltating sand with loess, at least until the landscape became loess covered. Cryoturbation occurring immediately post-deglaciation may also be a factor in central Sweden. In any case, Schaetzl and Luehmann (2013) argue that the specific processes causing potential mixing are unclear; pedogenic processes, strong winds during deposition, cryoturbation and bioturbation are all possibilities and likely cause underlying sediment to be mixed into the loess rather than vice versa. Notably, these processes did not seem to operate at Gräshöjden, which shows coarser particles, a close association with a specific dune ridge and younger Holocene luminescence ages (Figure 11). The reasons for this discrepancy are uncertain as, like Finnhöjden, Gräshöjden is underlain by sandy till, but potentially relate to the later deposition of the material at Gräshöjden, and likely reworking of sediment from adjacent dunes.

Overall, our data suggest it is possible that loess deposits are not as rare as previously though in Sweden. However, it is clear that these Swedish deposits are comparatively very thin and in part mixed with underlying sediments, which to some extent would explain the prevailing view that these deposits are rare or even non-existent. Thin Swedish loess may be partially explained by the fact that in Sweden, dust sources would only have been active for a few thousand years during deglaciation, and previous loess deposits entirely removed by glacial erosion. This history contrasts with the situation in, for example, Alaska, where loess deposits extend back 3 Ma in the ice-free interior (Nadin et al., 2022), consistently fed by nearby active dust sources. However, our new ages suggest dust activity well into the middle Holocene, and the fact that other previously glaciated areas such as the northern part of the North European Plain show thicker loess deposits, demands further explanations for the thin loess in Sweden. Addressing this question requires a wider understanding of the true extent of these deposits beyond the two loess areas addressed in this study.

4.3 | Age of the loess: comparison with other aeolian archives in Sweden

As discussed above, there is no clear indication in the aliquot dose distributions that post-glacial quartz OSL ages from the loess samples are inaccurate estimates of the timing of loess deposition at the

10969837, 2022, 14, Downloaded from https://onlinelibrary.wiley.com/doi/10.1002/esp.5456 by CochraneItalia, Wiley Online Library on [19/12/2024]. See the Terms and Conditions (https://onlinelibrary.wiley.com/terms-and-conditions) on Wiley Online Library for rules of use; OA articles are governed by the applicable Creative Commons License

studied sites (Table 2, Figures 9–11). However, these ages are at times considerably younger than expected based on the majority (but not all) of previous work on associated dune sediments and a few ages taken from close by loess deposits (Alexanderson & Fabel, 2015; Lundqvist & Mejdahl, 1987) (Figure 14). Furthermore, soil-forming processes and mixing may complicate interpretation of luminescence ages taken from upper layers or thin loess and sand deposits (Hanson et al., 2015; Schaetzl et al., 2014). Currently, then, we cannot definitively differentiate between either possibility that the luminescence ages are comprised by soil-mixing processes, or that aeolian silt deposition occurred into the mid-Holocene at the study sites.

Previous work by Lundqvist and Mejdahl (1987) presented K-feldspar TL ages from two loess samples of undocumented depth; one each from Hökberg and Finnhöjden. These samples yielded ages of 9.2 ± 0.7 and 9.0 ± 0.7 ka for silts at Hökberg and Finnhöjden, respectively, corrected for fading based on four weeks of storage. These ages are 1–2 ka younger than the local deglaciation at the sites (Stroeven et al., 2016) but in line with other dune ages from that work. Furthermore, they overlap with the main post-glacial dune OSL ages obtained recently by Alexanderson and Bernhardson (2019), and also with the majority of dune OSL ages for Brattforsheden in Alexanderson and Fabel (2015) (Figure 14). Indeed, Alexanderson and Fabel (2015) also present quartz OSL ages from aeolian silts at both Finnhöjden and Gräshöjden (taken at 55–45 cm depth in profiles) of 9.2 ± 0.6 and 9.6 ± 0.5 ka, respectively. While the TL ages of Lundqvist and Mejdahl (1987) may have a number of issues that limit age determination (Roberts, 2008), there is no reason to doubt the accuracy of the silt or dune quartz OSL ages provided by Alexanderson and Fabel (2015) and Alexanderson and Bernhardson (2019).

These published ages are consistent with the upper two ages presented here for the HB0101 profile at Hökberg (Figure 9). However, the ages presented here for Finnhöjden and Gräshöjden show a different pattern. While the lowermost reliable OSL age on loess from FH2 is 8.7 ± 0.5 ka and therefore also broadly overlaps with the published ages, the other loess ages from Finnhöjden and the Gräshöjden ages are all substantially younger (ranging from 7.9 to 4.7 ka). We cannot discount that these young ages may be a result of sediment mixing processes, although if this is the case then it is notable that this mixing appears not to have affected the ages at Hökberg or those published by Lundqvist and Mejdahl (1987) and Alexanderson and Fabel (2015). It is, however, also possible that the dated silt samples at 45–55 cm from sections in Brattforsheden by Alexanderson and Fabel (2015) may well have been mixed loess and till sediments, but this possibility would not explain the mismatch at Gräshöjden, where only Holocene ages are found (Table 2, Figure 11).

Examination of dose rates and D_e values for the silt samples from Finnhöjden and Gräshöjden published in Alexanderson and Fabel (2015) shows that the dose rate values presented tend to be lower by c. 0.5 Gy ka^{-1} (Table 2). The reason for this discrepancy is unclear; water contents chosen in the two studies are similar, and in any case, to obtain a better age match between the studies would require that our dose rates were lower, implying impossible water content levels over saturation. Possibly dose rate estimation errors may be a factor in one or both studies, but other studies have demonstrated general consistency in dose rates between different techniques (Bate et al., 2017; Stevens et al., 2007) and in any case, if the ages matched between the studies this would mean a greater difference in dose rates reported by the two studies at the same sites. Differences in the accuracy of D_e determination may also be a factor, but given that all internal tests and adequate SAR parameter tests have been satisfactorily performed in both studies, and the fact that these sediments appear to be ideal candidates for quartz SAR OSL dating (Alexanderson, 2022; Alexanderson & Murray, 2012), there is no evidence for D_e determination error beyond the age differences themselves.

Notwithstanding the possibility of sediment mixing in thin loess generally, the new and previously published ages may suggest a wide time window of loess deposition in central Sweden (Figure 14). At Hökberg, the two upper ages (Figure 9) are in line with an approximate deglaciation age of c. 11 ka (Stroeven et al., 2016) and suggest extremely rapid and short-lived dust activity directly after ice retreat from the area. These ages fit in with evidence that the majority of aeolian activity in southern-central Sweden occurred at c. 11–8 ka

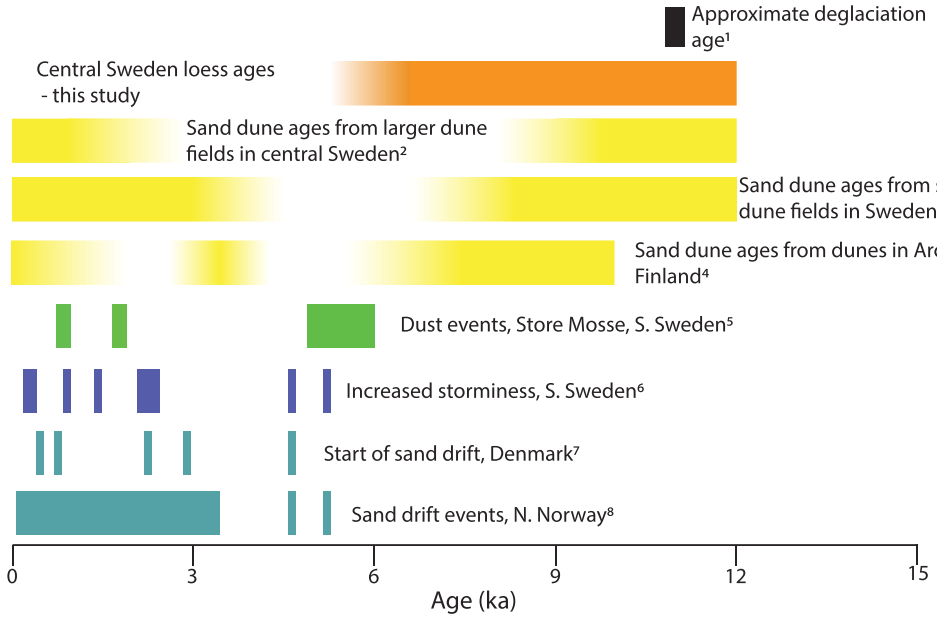

FIGURE 14 Approximate range of depositional ages for loess presented in this study, alongside approximate timing of local deglaciation and phases of independently dated aeolian sediment activity in Fennoscandia. 1 = Stroeven et al. (2016), 2 = Bernhardson et al. (2019); 3 = Alexanderson and Bernhardson (2019); 4 = Matthews and Seppälä (2014); 5 = Kylander et al. (2016); 6 = De Jong et al. (2006); 7 = Clemmensen et al. (2009); 8 = Nielsen et al. (2016) [Color figure can be viewed at wileyonlinelibrary.com]

10969837, 2022, 14, Downloaded from https://onlinelibrary.wiley.com/doi/10.1002/esp.5456 by CochraneItalia, Wiley Online Library on [19/12/2024]. See the Terms and Conditions (https://onlinelibrary.wiley.com/terms-and-conditions) on Wiley Online Library for rules of use; OA articles are governed by the applicable Creative Commons License

(Figure 14), prior to forest development and land stabilization (e.g. Bernhardson et al., 2019). This period would be characterized by high wind speeds, sediment supplies and availability, fuelled by sediment-rich meltwater from the retreating ice sheet and a land surface devoid of stabilizing forest cover, and also potentially relatively high wind speeds around the retreating ice mass.

By contrast, though, taking the luminescence ages at face value, aeolian activity at Finnhöjden may have extended to at least c. 6 ka (Figure 10), and at Gräshöjden sediment movement may not have started until around 8 ka and extended to at least c. 5 ka (Figure 11). The timing of this corresponds to the generally warm and wet Atlantic/Northgrippian stages of the Holocene. As noted above, soil formation, pedoturbation and root penetration may in some instances have led to underestimates of sediment depositional ages (cf. Bateman et al., 2007; Hanson et al., 2015; Stevens et al., 2008). However, the consistency of ages between close by sections, the lack of age inversions (except with one age at GH2; Figure 11), the relatively low OD values (Table 1), analysis of the dose distributions above, the lack of any obvious reworking structures in the loess sediment and the fact that at HB0101 the OSL ages are consistent with deglaciation (Figure 9), all point against this possibility. On the other hand, published middle and early to mid-Holocene aeolian sand movement ages are relatively rare in southern Sweden (Alexanderson & Bernhardson, 2019) (Figure 14). These published results imply limited aeolian activity over much of the period between 8 and 3 ka, although the existence of some mid-Holocene luminescence ages on dunes suggests that aeolian activity did sporadically occur (Figure 14). Furthermore, much of the aeolian activity at Finnhöjden and Gräshöjden reported here occurred prior to inferred episodes of increased storminess in NW Europe and Sweden from c. 5.5 ka (De Jong et al., 2006; Sorrel et al., 2012), as well as sand drift in Denmark and north Norway (Clemmensen et al., 2009; Nielsen et al., 2016) (Figure 14). Finer dust accumulated in peat from the Store Mosse peat bog increases at c. 6.4 cal kyr BP (Kylander et al., 2016), but even this activity also post-dates much of the accumulation at Finnhöjden and Gräshöjden (Figure 14).

In contrast, reactivation of sand dunes and deposition of reworked sand blowouts in Arctic Finland appears to have occurred from ~8.3 cal kyr BP and may be linked to forest or tundra fire activity (Matthews & Seppälä, 2014). This pattern matches much more closely the record of aeolian activity seen here in the loess from central Sweden (Figure 14). However, the central Sweden loess deposits so far lack any discrete charcoal bands that might suggest a similar mechanism driving aeolian activity. It is worth noting that at Gräshöjden especially, the relatively coarse size of the 'loess' sediments and geomorphic association with local sand dune ridges means these sediments are potentially better interpreted as a finer aeolian facies of sediments blown from nearby dune ridges, perhaps due to periodic dune destabilization (Figure 4) (e.g. Schaetzl et al., 2021). Indeed, at Finnhöjden, although the silt sediments are finer grained and closer to classic loess in texture (Figure 12), they also grade laterally into cover sands and ultimately dunes further downhill (Figure 4). This close association suggests that, if accurate, the relatively younger ages of the silts may be due to formation under periodic Holocene blowouts of nearby dunes and cover sands and increased finer sediment supply uphill from these source areas. This explanation would generally be compatible with the older OSL ages from the main dunes reported in Alexanderson and Fabel (2015), as long as these ages were from the cores of the dunes rather than reactivated blowouts.

Overall, at present we cannot rule out the possibility that soil-mixing processes would have led to the mid-Holocene ages for the studied Brattforsheden loess sections, but nor can we exclude the possibility that our data reveal aeolian activity in central Sweden through the Holocene (Figure 14), in response to periodic destabilization of dunes and land surfaces. In this latter scenario, the location of the loess above the highest shoreline would have no meaning for the deposit age, as the relatively high depositional location for loess is simply due to geomorphic controls on the texture of aeolian sedimentary facies. It is unclear to what extent any mid-Holocene aeolian loess activity was restricted to a small area, or a wider feature. However, the consistency of the Holocene loess ages across multiple, separated sites at Brattforsheden may hint at wider-scale processes. We also note that the existence of open sand patches since at both Brattforsheden and Bonäsheden, throughout the Holocene, is indicated by the presence of sand lizards at both sites (*Lacerta agilis*), a relic from the early Holocene (Berglind, 2005). However, we emphasize that this is a working hypothesis, and more detailed dating of loess, cover sands and nearby dune cores and drapes is required to fully address this apparent age mismatch between the loess here and other aeolian activity in southern Sweden.

4.4 | Sources, associations and wind directions

Our mapping shows that aeolian silts have a very close association with cover sands and dunes. Indeed, the loess deposits often grade into the coarser aeolian sediments, downhill and closer to glaciofluvial systems, implying continuous elevation and distance-driven size sorting of sand and silt particles away from likely glaciofluvial source areas. The close association with dunes means that any aeolian reworking of these sediments into loess would have been relatively short distance (several kilometres) and as such there would have been limited longer-range transport of coarse dust particles in the atmosphere during phases of deposition. There would therefore have been limited direct radiative forcing effects from this coarse dust, but its deposition locally may have impacted albedo and certainly soil types.

However, given that many OSL ages from the loess deposits are much younger than the Fennoscandian Ice Sheet retreat (Figure 14), this implies that not all of the silt was transported directly to final deposition from the active glaciofluvial systems or exposed tills during the deglaciation. Later transport may have occurred due to reworking of till, dune or cover sand deposits. If reliable, the younger loess ages complicate interpretation of possible wind directions during loess transport in relation to dune form, as well as interpretation of the orientation of loess deposits in relation to glaciofluvial deposits, and means the impact of this coarse dust movement would have been spread out in time rather than focused on a short period during deglaciation. Determining the extent of loess deposits in Sweden and the timing of their movement more widely will allow records of this dust activity to be included in dust load modelling for the Holocene, where records from Fennoscandia are currently rare (Albani et al., 2015).

In any case, there is a clear tendency for loess to be found on higher ground, above the main dune areas, and to the south and southwest of major glaciofluvial channels and dune fields (Figures 2

10969837, 2022, 14, Downloaded from https://onlinelibrary.wiley.com/doi/10.1002/esp.5456 by CochraneItalia, Wiley Online Library on [19/12/2024]. See the Terms and Conditions (https://onlinelibrary.wiley.com/terms-and-conditions) on Wiley Online Library for rules of use; OA articles are governed by the applicable Creative Commons License

and 3). With the exception of Gräshöjden, the loess deposits grade to cover sands downslope to the north and east and show general trends towards coarsening and thickening in these directions too (Figures 4 and 5). However, these relationships are complex as loess also becomes coarser and thicker closer to sandy areas at Hökberg and Gräshöjden, irrespective of direction, while steep slopes are devoid of loess (Figures 4 and 5). Thus the distribution of loess is partly a function of topography and partly proximity to sand deposits and glaciofluvial sources. This situation is highly reminiscent of those in other areas of thin loess cover in association with sand, especially as recently documented by Schaetzl et al. (2021) for Holocene dune-proximal loess in northern Michigan. Here, too, loess was locally sourced and deposited on higher ground close to sand dunes at lower elevations, where it grades to finer grain sizes away from the dunes. Schaetzl et al. (2021) conclude that silt generation occurred during sand saltation and these finer particles were transported to higher elevations where they were deposited. These loess deposits are Holocene in age, similar to much of the loess here, if the luminescence results are accurate, and we argue that similar processes may also have occurred in central Sweden. However, as SEM images from the loess provide no support for extended saltation transport or silt production in dunes, in the central Swedish case it is quite likely that abundant silts were already present in the dunes, tills and glaciofluvial outwash (Figure 13). The thin loess cover in northeastern Wisconsin also shows a clear fining trend, downwind away from outwash plain source areas (Schaetzl & Attig, 2013).

We presume that aeolian silt transport would have been quite widespread downwind of sand dunes over all the areas studied here, but that deposition and preservation tended to only occur on higher ground because of the effects of saltating sand grains preventing loess deposition (as e.g. in the last glacial loess of the Upper Mississippi River in the continental USA; Mason et al., 1999). Here, sand movement was restricted to valleys due to the topographic obstacle of the steeper slopes on valley sides. However, those same sand grains that prevented loess deposition in valley areas would have acted to mobilize the loess-forming silts (Bagnold, 1941) also found in tills and glaciofluvial sediments of the study areas. At present we cannot say whether the glaciofluvial, dune or till sediments would have been the dominant source for the loess, but note that the strong grading of dunes through cover sand to loess with elevation, away from glaciofluvial systems, hints that the ultimate source may have been the glaciofluvial sediments, potentially alongside extensive reworking from dunes.

Irrespective of these relationships, suitable topographic highs to the north and east of the glaciofluvial valley systems exist in some of the study areas but strikingly contain no loess (especially around the area west of Bonäsheden; Figure 5), in contrast to the higher areas to the south and southwest. This pattern clearly points to dust transporting winds from the north and northeast. We also note that wind-tunnel experiments on dust transport suggest that dust deposition occurs both on the lee and stoss side of an obstruction, but that stoss deposits were coarser and lee deposits finer than the average (Goossens, 1996, 2006). While very different in scale to the wind-tunnel experiments, this observation is somewhat reminiscent of the pattern in loess thickness and coarseness seen at Finnhöjden and west of Bonäsheden (Figures 4 and 5), again implying predominant transport from the northeast.

However, it is important to note that because few suitable topographic highs (above the main area of sand saltation in the valleys) exist to the southeast, wider transport of dust sediment from the northwest cannot be ruled out by these patterns. Indeed, at Gräshöjden (Figure 4C) an area of coarse loess and cover sand occurs to the southeast of a sand dune area, where dune crests are generally oriented SW–NE, indicating transport of dust to the southeast by northwest winds. A complication here is the possible different timing of loess deposition in the different areas, and compared to the dune ages (Figure 14), but at Gräshöjden the loess (cover sand) distribution seems to fit with NW winds, implying the deposit comprises finer or reworked sediments of the dune sands that lie to the northwest.

Despite this evidence for transport from the NW at Gräshöjden, our results generally reinforce the previously highlighted inconsistencies between parabolic dune orientation (indicating NW winds; e.g. Bernhardson et al., 2019) and loess deposit position (dominantly indicting NE winds; e.g. Hjulström et al., 1955). However, surface NE wind transport for the loess is hard to reconcile with the potentially relatively young age (Holocene) of some of the Finnhöjden loess deposits (Figure 10). During the Holocene, no ice sheet would have been present to facilitate significant NE winds, either via ice sheet anticyclones or deflected katabatic winds. Indeed, the modern geostrophic wind regime in central and southern Sweden is dominated by westerly winds (Bergström & Söderberg, 2008), which at surface level would be affected by the NW–SE trending valley systems in central Sweden, leading to dominant northwesterly surface winds. Modern surface wind observational data from meteorological stations close to the sample sites clearly shows the dominance of westerly components to the wind field, both for all wind speeds and those over 5 m s^{-1} (Figure S4). Furthermore, the more N–S directed valleys at Brattforsheden are reflected in more N–S dominant wind directions there, while the NW–SE directed valleys west of Bonäsheden show stronger westerly components to surface winds. This topographic control on winds is consistent with observations of the orientation of parabolic dunes in multiple areas over central and southern Sweden, mostly formed in the 1000–3000 years post-deglaciation (Figure 14), and pointing to W and NW winds even with the Fennoscandian Ice Sheet still present (Bernhardson et al., 2019).

As such, the reason for the discrepancy between distribution of loess and dune orientations remains unresolved. Ekman flow remains one explanation (Hjulström et al., 1955), yet requires significant further testing. The effect of Ekman flow in the atmosphere may be felt as low as 20–100 m above the surface (Constantin & Johnson, 2019), which would be consistent with this effect driving deflection of dominant NW surface winds to the right (south or southeast) along the hills in both study areas as elevation increases. This deflection of higher-level winds that probably transported silt particles could theoretically produce the loess distribution patterns seen in Figures 2 and 3, the lack of loess to the northeast and east of glaciofluvial systems, and allow for dust transport also to the southeast at Gräshöjden. In the valley bottoms, the dominant orientation of dune crests would also still be a function of the same northwesterly surface winds that were deflected south and southeast at higher levels. However, this hypothesis is only tentative and a major step towards resolving the discrepancy in inferred wind directions is through more detailed constraint of the timing and patterns of dune and loess formation and modification more widely in Sweden.

10969837, 2022, 14, Downloaded from https://onlinelibrary.wiley.com/doi/10.1002/esp.5456 by CochraneItalia, Wiley Online Library on [19/12/2024]. See the Terms and Conditions (https://onlinelibrary.wiley.com/terms-and-conditions) on Wiley Online Library for rules of use; OA articles are governed by the applicable Creative Commons License

5 | CONCLUSIONS

Analysis of silts associated with dunes and close to former glaciofluvial systems draining the decaying Fennoscandian Ice Sheet in central Sweden confirms that these deposits are loess. Our mapping around Brattforsheden and west of Bonäsheden extends the area of known loess coverage in these areas, and demonstrates the clear topographic control on aeolian facies, with sand dunes at lower elevation grading to cover sands and then silty loess on hill tops. However, the basal sediments of these loess deposits are mixed with underlying sandy till material, as also described where till underlies thin loess deposits in North America. Our results also point to the possibility of more extensive loess deposits in Sweden than previously believed.

OSL dating of quartz in loess deposits here suggests mostly Holocene ages, ranging from immediately post-deglaciation through to c. 5 ka. The OSL ages pass all internal tests and show good fast component-dominated signals. While the possibility of soil mixing causing erroneously young ages cannot be discounted, analysis of dose distributions does not provide support for such processes affecting the ages. If taken as reliable, these results would greatly extend the age range of aeolian activity in these regions and suggest that periodic landscape destabilization may have reactivated dunes or deflated silty, sandy tills underlying the loess areas. Such a reactivation pattern has also been observed in Arctic Finland but has not earlier been reported for loess in central and southern Sweden. Pre-deglacial OSL ages are interpreted as overestimates due to mixing of loess with underlying sandy till, either syn- or post-depositionally. We note, however, that further testing is required to fully constrain the potential influence of soil formation and mixing on ages in these thin loess deposits.

Finally, the results here reinforce the clear spatial patterns in loess coverage; hills to the north and northeast of glaciofluvial valley systems (the presumed loess source areas) are loess-free, while loess extensively covers hills to the south and southwest. This pattern suggests loess transport by NE winds, but is inconsistent with wind directions inferred from dune morphology and loess ages. The reasons for this discrepancy are currently unclear, but the hypothesis of Hjulström et al. (1955) that the pattern is likely the result of Ekman flow effects on transport of coarse dust particles transported to higher elevations is one possible scenario. Under this model, dominant topographically controlled NW winds during and immediately after deglaciation, as well as in the Holocene, would be deflected to the south and southeast by Coriolis force at higher elevations (even just tens of metres above the surface) where the silts are transported, leading to the striking patterns in loess coverage. These loess deposits are source proximal, and their geographic spread points to transport from sources just a few kilometres away, implying this Ekman flow effect would need to have operated at very low levels in the atmosphere. Fine dust particles were no doubt produced too, and transported further afield, but would have been relatively limited in volume. However, we emphasize that this hypothesis and other potential explanations require further testing in other loess areas, and indeed the extent of Holocene coarse dust transport in Sweden now needs careful, detailed analysis through dating of multiple aeolian archives.

ACKNOWLEDGEMENTS

This research was funded by the Swedish Geological Survey (Grant No. 6-1857/2020) and the Swedish Research Council (VR Grant No. 2017-03888). We thank Vanda Jakabová and Caroline Morin for help in the laboratory and field. We are grateful to Salome Oehler for luminescence sample preparation and to Mark Johnson, Anna Hedeving, Fanny Ekström and Helena Alexanderson for informative discussions on Swedish loess. Rickard Pettersson is thanked for help with the GPS data and equipment. Two anonymous reviewers are thanked for their constructive comments that significantly improved the manuscript.

CONFLICT OF INTEREST

The authors have no conflict of interest to disclose.

AUTHOR CONTRIBUTIONS

All authors have contributed to the data acquisition and analysis, read the manuscript and made comments on the submitted version.

DATA AVAILABILITY STATEMENT

All luminescence data are available open access via tables in the paper. Other data are available on request from the authors.

ORCID

Thomas Stevens https://orcid.org/0000-0002-6662-6650

REFERENCES

Adebiyi, A.A. & Kok, J.F. (2020) Climate models miss most of the coarse dust in the atmosphere. *Science Advances*, 6(15), eaaz9507.

Agrell, H. & Hultman, R. (1971) Deposits of wind-blown silt in the north-eastern part of the southern Swedish uplands. *GFF*, 93, 231–235.

Albani, S., Mahowald, N.M., Winckler, G., Anderson, R.F., Bradtmiller, L.I., Delmonte, B. et al. (2015) Twelve thousand years of dust: The Holocene global dust cycle constrained by natural archives. *Climate of the Past*, 11(6), 869–903. Available from: https://doi.org/10.5194/cp-11-869-2015

Alexanderson, H. (2022) Luminescence characteristics of Scandinavian quartz, their connection to bedrock provenance and influence on dating results. *Quaternary Geochronology*, 69, 101272. Available from: https://doi.org/10.1016/j.quageo.2022.101272

Alexanderson, H. & Bernhardson, M. (2016) OSL dating and luminescence characteristics of aeolian deposits and their source material in Dalarna, central Sweden. *Boreas*, 45(4), 876–893. Available from: https://doi.org/10.1111/bor.12197

Alexanderson, H. & Bernhardson, M. (2019) Late glacial and Holocene sand drift in northern Götaland and Värmland, Sweden: Sediments and ages. *GFF*, 141(2), 84–105. Available from: https://doi.org/10.1080/11035897.2019.1582559

Alexanderson, H., Bernhardson, M. & Kalińska-Nartiša, E. (2016) *Aeolian Activity in Sweden: An Unexplored Environmental Archive*, LUNDQUA Report No. 42. Lund: Department of Geology, Lund University.

Alexanderson, H. & Fabel, D. (2015) Holocene chronology of the Brattforsheden delta and inland dune field, SW Sweden. *Geochronometria*, 42(1), 1–16. Available from: https://doi.org/10.1515/geochr-2015-0001

Alexanderson, H. & Murray, A.S. (2012) Problems and potential of OSL dating Weichselian and Holocene sediments in Sweden. *Quaternary Science Reviews*, 44, 37–50. Available from: https://doi.org/10.1016/j.quascirev.2009.09.020

Arnold, L.J. & Roberts, R.G. (2009) Stochastic modelling of multi-grain equivalent dose (D_e) distributions: Implications for OSL dating of sediment mixtures. *Quaternary Geochronology*, 4(3), 204–230. Available from: https://doi.org/10.1016/j.quageo.2008.12.001

Bagnold, R.A. (1941) *The Physics of Blown Sand and Desert Dunes*. London: Chapman & Hall.

10969837, 2022, 14, Downloaded from https://onlinelibrary.wiley.com/doi/10.1002/esp.5456 by CochraneItalia, Wiley Online Library on [19/12/2024]. See the Terms and Conditions (https://onlinelibrary.wiley.com/terms-and-conditions) on Wiley Online Library for rules of use; OA articles are governed by the applicable Creative Commons License

Banak, A., Pavelić, D., Kovačić, M. & Mandic, O. (2013) Sedimentary characteristics and source of late Pleistocene loess in Baranja (eastern Croatia). *Aeolian Research*, 11, 129–139. Available from: https://doi.org/10.1016/j.aeolia.2013.08.002

Bate, S., Stevens, T., Buylaert, J.-P., Marković, S.B., Roos, P. & Tasić, N. (2017) Pottery versus sediment: Optically stimulated luminescence dating of the Neolithic Vinča culture, Serbia. *Quaternary International*, 429, 45–53. Available from: https://doi.org/10.1016/j.quaint.2014.09.042

Bateman, M.D., Boulter, C.H., Carr, A.S., Frederick, C.D., Peter, D. & Wilder, M. (2007) Detecting post-depositional sediment disturbance in sandy deposits using optical luminescence. *Quaternary Geochronology*, 2(1–4), 57–64. Available from: https://doi.org/10.1016/j.quageo.2006.05.004

Berglind, S.-Å. (2005) *Population dynamics and conservation of the sand lizard* (Lacerta agilis) *on the edge of its range*. PhD thesis, Uppsala University.

Bergström, H. & Söderberg, S. (2008) *Wind Mapping of Sweden: Summary of Results and Methods Used*, Rapport 1401-5706. Frederiksberg: Elforsk.

Bernhardson, M. & Alexanderson, H. (2017) Early Holocene dune field development in Dalarna, central Sweden: A geomorphological and geophysical case study. *Earth Surface Processes and Landforms*, 42(12), 1847–1859. Available from: https://doi.org/10.1002/esp.4141

Bernhardson, M. & Alexanderson, H. (2018) Early Holocene NW–W winds reconstructed from small dune fields, central Sweden. *Boreas*, 47(3), 869–883. Available from: https://doi.org/10.1111/bor.12307

Bernhardson, M., Alexanderson, H., Björck, S. & Adolphi, F. (2019) Sand drift events and surface winds in south-central Sweden: From the deglaciation to the present. *Quaternary Science Reviews*, 209, 13–22. Available from: https://doi.org/10.1016/j.quascirev.2019.01.017

Bradák, B., Seto, Y., Stevens, T., Ujvari, G., Feher, K. & Költringer, C. (2021) Magnetic susceptibility in the European loess belt: New and existing models of magnetic enhancement in loess. *Palaeogeography, Palaeoclimatology, Palaeoecology*, 569, 110329. Available from: https://doi.org/10.1016/j.palaeo.2021.110329

Bryant, I.D. (1982) Loess deposits in Lower Adventdalen, Spitsbergen. *Polar Research*, 2, 93–102.

Buggle, B., Glasser, B., Hambach, U., Gerasimenko, N. & Marković, S.B. (2011) An evaluation of geochemical weathering indices in loess-paleosol studies. *Quaternary International*, 240(1–2), 12–21. Available from: https://doi.org/10.1016/j.quaint.2010.07.019

Bullard, J.E., Baddock, M., Bradwell, T., Crusius, J., Darlington, E., Galero, D. et al. (2016) High-latitude dust in the earth system. *Reviews of Geophysics*, 54(2), 447–485. Available from: https://doi.org/10.1002/2016RG000518

Clemmensen, L.B., Murray, A., Heinemeier, J. & De Jong, R. (2009) The evolution of Holocene coastal dunefields, Jutland, Denmark: A record of climate change over the past 5000 years. *Geomorphology*, 105(3–4), 303–313. Available from: https://doi.org/10.1016/j.geomorph.2008.10.003

Cocco, F., Andreucci, S., Sechi, D., Cossu, G. & Funedda, A. (2019) Upper Pleistocene tectonics in western Sardinia (Italy): Insights from the Sinis peninsula structural high. *Terra Nova*, 31(5), 485–493. Available from: https://doi.org/10.1111/ter.12418

Constantin, A. & Johnson, R.S. (2019) Atmospheric Ekman flows with variable eddy viscocity. *Boundary-Layer Meterology*, 170(3), 395–414. Available from: https://doi.org/10.1007/s10546-018-0404-0

Cunningham, A.C. & Wallinga, J. (2010) Selection of integration time intervals for quartz OSL decay curves. *Quaternary Geochronology*, 5(6), 657–666. Available from: https://doi.org/10.1016/j.quageo.2010.08.004

Dahlberg, N. & Mikko, H. (2009) Map of the Quaternary Deposits 14E Mora SV, scale 1:100 000. Sveriges geologiska undersökning K 136.

De Jong, R., Björck, S., Björkman, L. & Clemmensen, L.B. (2006) Storminess variation during the last 6500 years as reconstructed from an ombrotrophic peat bog in Halland, southwest Sweden. *Journal of Quaternary Science*, 21(8), 905–919. Available from: https://doi.org/10.1002/(ISSN)1099-1417

Dearing, J., Dann, R.J.L., Hay, K., Lees, J.A., Loveland, P.J., Maher, B.A. et al. (1996) Frequency-dependent susceptibility measurements of environmental materials. *Geophysical Journal International*, 124(1), 228–240. Available from: https://doi.org/10.1111/j.1365-246X.1996.tb06366.x

Dietze, M., Kreutzer, S., Burow, C., Fuchs, M., Fischer, M. & Schmidt, C. (2016) The Abanico plot: Visualising chronometric data with individual standard errors. *Quaternary Geochronology*, 31, 12–18. Available from: https://doi.org/10.1016/j.quageo.2015.09.003

Duller, G.A.T. (2003) Distinguishing quartz and feldspar in single grain luminescence measurements. *Radiation Measurements*, 37(2), 161–165. Available from: https://doi.org/10.1016/S1350-4487(02)00170-1

Duller, G.A.T. (2008) Single-grain optical dating of Quaternary sediments: Why aliquot size matters in luminescence dating. *Boreas*, 37(4), 589–612. Available from: https://doi.org/10.1111/j.1502-3885.2008.00051.x

Ekström, F. & Hedeving, A. (2021) Loess in southwestern Sweden: Determining the genesis of the silt-rich layer rödfemman in Svartedalen nature reserve. MSc thesis, University of Gothenberg.

Ferranti, L., Burrato, P., Sechi, D., Andreucci, S., Pepe, F. & Pascuci, V. (2021) Late Quaternary coastal uplift of southwestern Sicily, central Mediterannean Sea. *Quaternary Science Reviews*, 255, 106812. Available from: https://doi.org/10.1016/j.quascirev.2021.106812

Fredén, C. (2001) Jordartskartan 11D Munkfors SO, 1:50 000. Sveriges geologiska undersökning Ae 150.

Fuchs, M., Woda, C. & Bürkert, A. (2007) Chronostratigraphy of a sediment record from the Hajar mountain range in North Oman: Implications for optical dating of insufficiently bleached sediments. *Quaternary Geochronology*, 2, 202–207.

Galbraith, R.F. & Roberts, R.G. (2012) Statistical aspects of equivalent dose and error calculation and display in OSL dating: An overview and some recommendations. *Quaternary Geochronology*, 11, 1–27.

Goossens, D. (1996) Wind tunnel experiments of eolian dust deposition along ranges of hills. *Earth Surface Processes and Landforms*, 21(3), 205–216. Available from: https://doi.org/10.1002/(SICI)1096-9837(199603)21:3<205::AID-ESP505>3.0.CO;2-T

Goossens, D. (2006) Eolian deposition of dust over hills: The effect of dust grain size on the deposition pattern. *Earth Surface Processes and Landforms*, 31(6), 762–776. Available from: https://doi.org/10.1002/esp.1272

Groot-Zwaaftink, C.D., Grythe, H., Skov, H. & Stohl, A. (2016) Substantial contribution of northern high-latitude sources to mineral dust in the Arctic. *Journal of Geophysical Research – Atmospheres*, 121(22), 13678–13697. Available from: https://doi.org/10.1002/2016JD025482

Guérin, G., Adamiec, G. & Aitken, M. (2011) Dose-rate conversion factors: Update. *Ancient TL*, 29, 37–50.

Guérin, G., Christophe, C., Philippe, A., Murray, A.S., Thomsen, K.J., Tribolo, C. et al. (2017) Absorbed dose, equivalent dose, measured dose rates, and implications for OSL age estimates: Introducing the average dose model. *Quaternary Geochronology*, 41, 163–173. Available from: https://doi.org/10.1016/j.quageo.2017.04.002

Hanson, P.R., Mason, J.A., Jacobs, P.M. & Young, A.R. (2015) Evidence for bioturbation of luminescence signals in eolian sand on upland ridgetops, southeastern Minnesota, USA. *Quaternary International*, 362, 108–115. Available from: https://doi.org/10.1016/j.quaint.2014.06.039

Hjulström, F., Sundborg, Å. & Falk, Å. (1955) Problems concerning the deposits of windblown silt in Sweden. *Geografiska Annaler*, 1–2, 86–117.

Hörner, N.G. (1927) *Brattforsheden ett värmländskt randdeltekomplex och dess dyner*. SGU C342. Geological Survey of Sweden: Uppsala.

Hrouda, F. (2011) Models of frequency-dependent susceptibility of rocks and soils revisited and broadened. *Geophysical Journal International*, 187(3), 1259–1269. Available from: https://doi.org/10.1111/j.1365-246X.2011.05227.x

Jackson, M.G., Oskarsson, N., Trønnes, R.G., McManus, J.F., Oppo, D.W., Grönvold, K. et al. (2005) Holocene loess deposition in Iceland: Evidence for millennial-scale atmosphere–ocean coupling in the

10969837, 2022, 14, Downloaded from https://onlinelibrary.wiley.com/doi/10.1002/esp.5456 by CochraneItalia, Wiley Online Library on [19/12/2024]. See the Terms and Conditions (https://onlinelibrary.wiley.com/terms-and-conditions) on Wiley Online Library for rules of use; OA articles are governed by the applicable Creative Commons License

North Atlantic. *Geology*, 33(6), 509–512. Available from: https://doi.org/10.1130/G21489.1

Klemsdal, T. (1969) Eolian forms in parts of Norway. *Norwegian Journal of Geography*, 23, 49–66.

Knippertz, P. & Stuut, J.-B.W. (2014) *Mineral Dust: A Key Player in the Earth System*. Dordrecht: Springer.

Kylander, M.E., Martínez-Cortizas, A., Bindler, R., Greenwood, S.L., Mörth, C.-M. & Rauch, S. (2016) Potentials and problems of building detailed dust records using peat archives: An example from store Mosse (the "great bog"), Sweden. *Geochimica et Cosmochimica Acta*, 190, 156–174. Available from: https://doi.org/10.1016/j.gca.2016.06.028

Kylander, M.E., Martínez-Cortizas, A., Bindler, R., Kaal, J., Sjöström, J., Hansson, S.V., Silva Sánchez, N. et al. (2018) Mineral dust as a driver of carbon accumulation in northern latitudes. *Scientific Reports*, 8(1), 6876. Available from: https://doi.org/10.1038/s41598-018-25162-9

Lehmkuhl, F., Nett, J.J., Pötter, S., Schulte, P., Sprafke, T., Jary, Z. et al. (2021) Loess landscapes of Europe – mapping, geomorphology, and zonal differentiation. *Earth-Science Reviews*, 215, 103496. Available from: https://doi.org/10.1016/j.earscirev.2020.103496

Lu, H., Wang, X., Wang, Y., Zhang, X., Yi, S., Wang, X. et al. (2022) Chinese loess and the Asian monsoon: What we know and what remains unknown. *Quaternary International*, 620, 85–97. Available from: https://doi.org/10.1016/j.quaint.2021.04.027

Luehmann, M.D., Peter, B., Connallon, C.B., Schaetzl, R.J., Smidt, S.J., Liu, W. et al. (2016) Loamy, two-storied soils on the outwash plains of southwestern lower Michigan: Pedoturbation of loess with the underlying sand. *Annals of the Association of American Geographers*, 106, 551–571.

Luehmann, M.D., Schaetzl, R.J., Miller, B.A. & Bigsby, M. (2013) Thin, pedoturbated and locally sourced loess in the western upper peninsula of Michigan. *Aeolian Research*, 8, 85–100. Available from: https://doi.org/10.1016/j.aeolia.2012.11.003

Lundqvist, J. & Mejdahl, V. (1987) Thermoluminescence dating of eolian sediments in central Sweden. *Geologiska föreningens i Stockholm förhandlingar*, 109, 147–158.

Mahaney, W.C. (1995) Glacial crushing, weathering and diagenetic histories of quartz grains inferred from scanning electron microscopy. In: Menzies, J. (Ed.) *Modern Glacial Environments – Processes, Dynamics and Sediments*. Butterworth-Heinemann: Oxford, pp. 487–506.

Mahaney, W.C. (2002) *Atlas of Sand Grain Surface Textures and Applications*. New York, USA: Oxford University Press.

Maher, B.A. & Taylor, R.M. (1988) Formation of ultrafine-grained magnetite in soils. *Nature*, 336(6197), 368–370. Available from: https://doi.org/10.1038/336368a0

Marković, S.B., Hambach, U., Stevens, T., Kukla, G.J., Heller, F., McCoy, W.D. et al. (2011) The last million years recorded at the Stari Slankamen (northern Serbia) loess–palaeosol sequence: Revised chronostratigraphy and long-term environmental trends. *Quaternary Science Reviews*, 30(9–10), 1142–1154. Available from: https://doi.org/10.1016/j.quascirev.2011.02.004

Mason, J.A., Nater, E.A., Zanner, C.W. & Bell, J.C. (1999) A new model of topographic effects on the distribution of loess. *Geomorphology*, 28(3–4), 223–236. Available from: https://doi.org/10.1016/S0169-555X(98)00112-3

Matthews, J.A. & Seppälä, M. (2014) Holocene environmental change in subarctic aeolian dune fields: The chronology of sand dune reactivation events in relation to forest fires, palaeosol development and climatic variations in Finnish Lapland. *The Holocene*, 24(2), 149–164. Available from: https://doi.org/10.1177/0959683613515733

Muhs, D.R. (2013) The geologic records of dust in the Quaternary. *Aeolian Research*, 9, 3–48. Available from: https://doi.org/10.1016/j.aeolia.2012.08.001

Murray, A.S. & Wintle, A.G. (2000) Luminescence dating of quartz using an improved single-aliquot regenerative-dose protocol. *Radiation Measurements*, 32(1), 57–73. Available from: https://doi.org/10.1016/S1350-4487(99)00253-X

Murray, A.S. & Wintle, A.G. (2003) The single aliquot regenerative dose protocol: Potential for improvements in reliability. *Radiation Measurements*, 37(4–5), 377–381. Available from: https://doi.org/10.1016/S1350-4487(03)00053-2

Nadin, E., Goddard, S., Benowitz, J. & O'Sullivan, P. (2022) Blowing in the late Cenozoic wind – detrital zircon river contributions to an interior Alaska loess deposit. *Quaternary Science Reviews*, 275, 107266. Available from: https://doi.org/10.1016/j.quascirev.2021.107266

Nesbitt, H.W. & Young, G.M. (1982) Early Proterozoic climates and plate motions inferred from major element chemistry of lutites. *Nature*, 299(5885), 715–717. Available from: https://doi.org/10.1038/299715a0

Nielsen, P.R., Dahl, S.O. & Jansen, H.L. (2016) Mid- to late Holocene aeolian activity recorded in a coastal dunefield and lacustrine sediments on Andøya, northern Norway. *The Holocene*, 26(9), 1486–1501. Available from: https://doi.org/10.1177/0959683616640050

Nordell, P.O. (1984) Dokumentation av istida landformer, isavsmältning och högsta kustlinje i Vånådalen och Orsasjöns randområden. *Information från länsstyrelsen i Kopparbergs län (Information from the County Board of Kopparberg County)*, N4, 133.

Okko, V. (1957) The second Salpausselkä at Jylisjärvi, east of Hämeelinna. *Fennia*, 81, 1–46.

Overland, J., Dunlea, E., Box, J.E., Corell, R., Forsius, M., Kattsov, V. et al. (2019) The urgency of Arctic change. *Polar Science*, 21, 6–13. Available from: https://doi.org/10.1016/j.polar.2018.11.008

Pécsi, M. (1991) Loess is not just the accumulation of dust. *Quaternary International*, 7–8, 1–21.

Porat, N., Faerstein, G., Medialdea, A. & Murray, A.S. (2015) Re-examination of common extraction and purification methods of quartz and feldspar for luminescence dating. *Ancient TL*, 33, 255–258.

Prescott, J.R. & Hutton, J.T. (1994) Cosmic ray contributions to dose rates for luminescence and ESR dating: Large depths and long-term time variations. *Radiation Measurements*, 23(2–3), 497–500. Available from: https://doi.org/10.1016/1350-4487(94)90086-8

Pye, K. (1995) The nature, origin and accumulation of loess. *Quaternary Science Reviews*, 14(7–8), 653–667. Available from: https://doi.org/10.1016/0277-3791(95)00047-X

Roberts, H.M. (2008) The development and application of luminescence dating to loess deposits: A perspective on the past, present and future. *Boreas*, 37(4), 483–507. Available from: https://doi.org/10.1111/j.1502-3885.2008.00057.x

Schaetzl, R.J. & Attig, J.W. (2013) The loess cover of northeastern Wisconsin. *Quaternary Research*, 79(2), 199–214. Available from: https://doi.org/10.1016/j.yqres.2012.12.004

Schaetzl, R.J., Bettis, E.A., Crouvi, O., Fitzsimmons, K.E., Grimley, D.A., Hambach, U. et al. (2018) Approaches and challenges to the study of loess – introduction to the LoessFest special issue. *Quaternary Research*, 89(3), 563–618. Available from: https://doi.org/10.1017/qua.2018.15

Schaetzl, R.J., Forman, S.L. & Attig, J.W. (2014) Optical ages on loess derived from outwash surfaces constrain the advance of the Laurentide ice sheet out of the Lake Superior Basin, USA. *Quaternary Research*, 81(2), 318–329. Available from: https://doi.org/10.1016/j.yqres.2013.12.003

Schaetzl, R.J. & Loope, W.L. (2008) Evidence for an eolian origin for the silt-enriched soil mantles on the glaciated uplands of eastern upper Michigan, USA. *Geomorphology*, 100(3–4), 285–295. Available from: https://doi.org/10.1016/j.geomorph.2008.01.002

Schaetzl, R.J. & Luehmann, M.D. (2013) Coarse-textured basal zones in thin loess deposits: Products of sediment mixing and/or paleoenvironmental change? *Geoderma*, 192, 277–285. Available from: https://doi.org/10.1016/j.geoderma.2012.08.001

Schaetzl, R.J., Nyland, K.E., Kasmerchak, C.S., Breeze, V., Kamoske, A., Thomas, S.E. et al. (2021) Holocene, silty-sand loess immediately downwind of dunes in northern Michigan, USA. *Physical Geography*, 42(1), 25–49. Available from: https://doi.org/10.1080/02723646.2020.1734414

Sechi, D., Andreucci, S., Stevens, T. & Pascucci, V. (2020) Age and significance of late Pleistocene *Lithophyllum byssoides* intertidal algal ridge, NW Sardinia, Italy. *Sedimentary Geology*, 400,

10969837, 2022, 14, Downloaded from https://onlinelibrary.wiley.com/doi/10.1002/esp.5456 by CochraneItalia, Wiley Online Library on [19/12/2024]. See the Terms and Conditions (https://onlinelibrary.wiley.com/terms-and-conditions) on Wiley Online Library for rules of use; OA articles are governed by the applicable Creative Commons License

105618. Available from: https://doi.org/10.1016/j.sedgeo.2020.105618

SGU. (2015) *Högsta kustlinjen*. Geological Survey of Sweden: Uppsala.

Smedley, R.K., Duller, G.A.T., Rufer, D. & Utley, J.E.P. (2020) Empirical assessment of beta dose heterogeneity in sediments: Implications for luminescence dating. *Quaternary Geochronology*, 56, 101052. Available from: https://doi.org/10.1016/j.quageo.2020.101052

Sorrel, P., Debret, M., Billeaud, I., Jaccard, S.L., McManus, J.F. & Tessier, B. (2012) Persistent non-solar forcing of Holocene storm dynamics in coastal sedimentary archives. *Nature Geoscience*, 5(12), 892–896. Available from: https://doi.org/10.1038/ngeo1619

Stevens, T., Armitage, S.J., Lu, H. & Thomas, D.S.G. (2007) Examining the potential of high-resolution OSL dating of Chinese loess. *Quaternary Geochronology*, 2(1–4), 15–22. Available from: https://doi.org/10.1016/j.quageo.2006.03.004

Stevens, T., Lu, H., Thomas, D.S.G. & Armitage, S.J. (2008) Optical dating of abrupt shifts in the Late Pleistocene east Asian monsoon. *Geology*, 36(5), 415–418. Available from: https://doi.org/10.1130/G24524A.1

Stevens, T., Sechi, D., Bradák, B., Orbe, R., Baykal, Y., Cossu, G. et al. (2020) Abrupt last glacial dust fall over southeast England associated with dynamics of the British–Irish ice sheet. *Quaternary Science Reviews*, 250, 106641. Available from: https://doi.org/10.1016/j.quascirev.2020.106641

Strand, K. & Immonen, N. (2010) Dynamics of the Barents–Kara ice sheet as revealed by quartz sand grain microtextures of the Late Pleistocene Arctic Ocean sediments. *Quaternary Science Reviews*, 29(25–26), 3583–3589. Available from: https://doi.org/10.1016/j.quascirev.2010.09.017

Strand, K., Passchier, S. & Näsi, J. (2003) Implications of quartz grain microtextures for onset of Eocene/Oligocene glaciation in Prydz Bay, ODP site 1166, Antarctica. *Palaeogeography, Palaeoclimatology, Palaeoecology*, 198(1–2), 101–111. Available from: https://doi.org/10.1016/S0031-0182(03)00396-1

Stroeven, A.P., Hättestrand, C., Kleman, J., Heyman, J., Fabel, D., Fredin, O. et al. (2016) Deglaciation of Fennoscandia. *Quaternary Science Reviews*, 147, 91–121. Available from: https://doi.org/10.1016/j.quascirev.2015.09.016

Svedlund, J.-O. (2008a) Map of the Quaternary deposits 14E Mora NO, scale 1:100 000. Sveriges geologiska undersökning K 129.

Svedlund, J.-O. (2008b) Map of the Quaternary deposits 14E Mora NV, scale 1:100 000. Sveriges geologiska undersökning K 128.

Svedlund, J.-O. & Dahlberg, N. (2009) Map of the Quaternary deposits 14E Mora SO, scale 1:100 000. Sveriges geologiska undersökning K 137.

Thomsen, K.J., Murray, A.S., Buylaert, J.P., Jain, M., Hansen, J.H. & Aubry, T. (2016) Testing single-grain quartz OSL methods using sediment samples with independent age control from the Bordes-Fitte rockshelter (Roches d'Abilly site, central France). *Quaternary Geochronology*, 31, 77–96. Available from: https://doi.org/10.1016/j.quageo.2015.11.002

Trewin, N. (1988) Use of scanning electron microscope in sedimentology. In: Tucker, M.E. (Ed.) *Techiques in Sedimentology*. Oxford: Blackwell Scientific, pp. 229–273.

Újvári, G., Kok, J.F., Varga, G. & Kovács, J. (2016) The physics of wind-blown loess: Implications for grain size proxy interpretations in quaternary palaeoclimate studies. *Earth-Science Reviews*, 154, 247–278. Available from: https://doi.org/10.1016/j.earscirev.2016.01.006

Vandenberghe, D., De Corte, F., Buylaert, J.P., Kučera, J. & Van den Haute, P. (2008) On the internal radioactivity in quartz. *Radiation Measurements*, 43(2–6), 771–775. Available from: https://doi.org/10.1016/j.radmeas.2008.01.016

Vandenberghe, J. (2013) Grain size of fine-grained windblown sediment: A powerful proxy for process identification. *Earth-Science Reviews*, 121, 18–30. Available from: https://doi.org/10.1016/j.earscirev.2013.03.001

Vandenberghe, J. & Nugteren, G. (2001) Rapid climatic changes recorded in loess successions. *Global and Planetary Change*, 28(1–4), 1–9. Available from: https://doi.org/10.1016/S0921-8181(00)00060-6

Willemse, N.W., Koster, E.A., Hoogakker, B. & van Tatenhove, F.G.M. (2003) A continuous record of Holocene eolian activity in West Greenland. *Quaternary Research*, 59(3), 322–334. Available from: https://doi.org/10.1016/S0033-5894(03)00037-1

Wintle, A.G. & Murray, A.S. (2006) A review of quartz optically stimulated luminescence characteristics and their relevance in single-aliquot regeneration dating protocols. *Radiation Measurements*, 41(4), 369–391. Available from: https://doi.org/10.1016/j.radmeas.2005.11.001

Wright, J.S. (2007) An overview of the role of weathering in the production of quartz silt. *Sedimentary Geology*, 202(3), 337–351. Available from: https://doi.org/10.1016/j.sedgeo.2007.03.024

SUPPORTING INFORMATION

Additional supporting information can be found online in the Supporting Information section at the end of this article.

How to cite this article: Stevens, T., Sechi, D., Tziavaras, C., Schneider, R., Banak, A., Andreucci, S. et al. (2022) Age, formation and significance of loess deposits in central Sweden. *Earth Surface Processes and Landforms*, 47(14), 3276–3301. Available from: https://doi.org/10.1002/esp.5456

10969837, 2022, 14, Downloaded from https://onlinelibrary.wiley.com/doi/10.1002/esp.5456 by CochraneItalia, Wiley Online Library on [19/12/2024]. See the Terms and Conditions (https://onlinelibrary.wiley.com/terms-and-conditions) on Wiley Online Library for rules of use; OA articles are governed by the applicable Creative Commons License